J|A|C|S

A R T I C L E S

Electronic Structure, Chemical Bond, and Optical Spectra of Metal Bis(porphyrin) Complexes: A DFT/TDDFT Study of the Bis(porphyrin)M(IV) (M = Zr, Ce, Th) Series

Giampaolo Ricciardi,*,† Angela Rosa,*,† Evert Jan Baerends,*,‡ and Stan A. J. van Gisbergen‡

Contribution from Dipartimento di Chimica, Università della Basilicata, Via N. Sauro 85, 85100 Potenza, Italy, and Afdeling Theoretische Chemie, Vrije Universiteit, De Boelelaan 1083, 1081 HV Amsterdam, The Netherlands

Abstract: The electronic absorption spectra of the bis(porphyrin) sandwich complexes of the metals Zr, Ce, and Th are studied with time-dependent density functional theory (TDDFT). A ground-state electronic structure analysis reveals that the highest occupied one-electron levels are, as expected, composed of the porphyrin a_{1u} and a_{2u} highest occupied orbitals (the Gouterman orbitals), but the level pattern is not simply a pair of low-lying nearly degenerate in-phase combinations and a pair of high-lying approximately degenerate antibonding combinations. Instead, the a_{1u} split strongly and the a_{2u} do not. Since the calculated spectrum agrees very well with experiment, the assignment leaves little doubt that although the experimental spectrum has porphyrin-like features, such as the well-known Q and B bands, the actual composition of the states is rather different from that in porphyrin. In particular the strong mixing of $a_{1u} \rightarrow e_g^*$ and $a_{2u} \rightarrow e_g^*$ is absent, there is mixing with excitations of non-Gouterman type, and, in Ce, ring to metal charge-transfer transitions play an important role. The composition of the states as calculated in this work does not lead to a classification of the excitations as purely "excitonic" or "charge-resonance".

1. Introduction

Bis(porphyrin)metal(IV) complexes have been extensively studied in recent years[1−22] because of their structural, chemical, and spectroscopic similarity to the "special pair" found in the reaction center of photosynthetic bacteria.[23] The metal ion in bis(porphyrin) complexes holds the macrocycles closer than their van der Waals distance, resulting in strong $\pi-\pi$ interactions that mimic the electronic interactions occurring within the

special pair which are thought to be responsible for some of its peculiar properties, such as the ease of porphyrin π-system oxidation and the low energy of the first singlet ($\pi\pi^*$) excited state compared to corresponding monomeric chromophores. This latter property produces a bathochromic shift of the long-wavelength absorption band and makes the dimer an effective trap for the harvested photon energy. Bis(porphyrin)metal(IV) complexes have characteristic optical properties that include (i) momomer-like ground-state absorption features, the Q and B bands, the latter being slightly blue shifted compared to the monomer, (ii) Q″ and Q′ absorption bands at higher and lower energy than the monomer Q-bands, respectively, (iii) a broad weak Q′ fluorescence band substantially red shifted from the Q′ absorption maximum, and (iv) a phosphorescence band significantly red shifted from those of typical monoporphyrin complexes. The position of the Q′ and Q″ absorptions varies with the ionic radius of the metal and thus with the distance

* To whom correspondence should be addressed. E-mails: (G.R.) rg010sci@unibas.it, (A.R.) rosa@unibas.it, (E.J.B.) baerends@chem.vu.nl.
† Università della Basilicata.
‡ Vrije Universiteit.

(1) Bilsel, O.; Rodriguez, J.; Holten, D.; Girolami, G. S.; Milam, S. N.; Suslick, K. S. *J. Am. Chem. Soc.* **1990**, *112*, 4075.
(2) Bilsel, O.; Rodriguez, J.; Holten, D. *J. Phys. Chem.* **1990**, *94*, 3508.
(3) Bilsel, O.; Buchler, J. W.; Hammerschmitt, P.; Rodriguez, J.; Holten, D. *Chem. Phys. Lett.* **1991**, *182*, 415.
(4) Bilsel, O.; Rodriguez, J.; Milam, S. N.; Gorlin, P. A.; Girolami, G. S.; Suslick, K. S.; Holten, D. *J. Am. Chem. Soc.* **1992**, *114*, 6528.
(5) Bilsel, O.; Milam, S. N.; Girolami, G. S.; Suslick, K. S.; Holten, D. *J. Phys. Chem.* **1993**, *97*, 7216.
(6) Buchler, J. W.; Elsässer, K.; Kihn-Botulinski, M.; Scharbert, B. *Angew. Chem., Int. Ed. Engl.* **1986**, *25*, 286.
(7) Buchler, J. W.; Hüttermann, J.; Löffler, J. *Bull. Chem. Soc. Jpn.* **1988**, *61*, 71.
(8) Buchler, J. W.; De Cian, A.; Fischer, J.; Kihn-Botulinski, M.; Weiss, R. *Inorg. Chem.* **1988**, *27*, 339.
(9) Buchler, J. W.; Scharbert, B. *J. Am. Chem. Soc.* **1988**, *110*, 4272.
(10) Buchler, J. W.; De Cian, A.; Fischer, J.; Hammerschmitt, P.; Löffler, J.; Scharbert, B.; Weiss, R. *Chem. Ber.* **1989**, *122*, 2219.
(11) Buchler, J. W.; De Cian, A.; Fisher, J.; Hammerschmitt, P.; Weiss, R. *Chem. Ber.* **1991**, *124*, 1051.
(12) Buchler, J. W.; De Cian, A.; Elschner, S.; Fischer, J.; Hammerschmitt, P.; Weiss, R. *Chem. Ber.* **1992**, *125*, 107.
(13) Buchler, J. W.; Kihn-Botulinski, M.; Löffler, J.; Scharbert, B. *New J. Chem.* **1992**, *16*, 545.
(14) De Cian, A.; Moussavi, M.; Fischer, J.; Weiss, R. *Inorg. Chem.* **1985**, *24*, 3162.
(15) Girolami, G. S.; Milam, S. N.; Suslick, K. S. *Inorg. Chem.* **1987**, *26*, 343.
(16) Girolami, G. S.; Milam, S. M.; Suslick, K. S. *J. Am. Chem. Soc.* **1988**, *110*, 2011.
(17) Yan, X.; Holten, D. *J. Phys. Chem.* **1988**, *92*, 409.
(18) Kadish, K. M.; Moninot, G.; Hu, Y.; Dubois, D.; Ibnlfassi, A.; Barbe, J.-M.; Guilard, R. *J. Am. Chem. Soc.* **1993**, *115*, 8153.
(19) Kim, K.; Lee, W. S.; Kim, H.-J.; Cho, S.-H.; Girolami, G. S.; Gorlin, P. A.; Suslick, K. S. *Inorg. Chem.* **1991**, *30*, 2652.
(20) Kim, H.-J.; Whang, D.; Kim, J.; Kim, K. *Inorg. Chem.* **1992**, *31*, 3882.
(21) Donohoe, R. J.; Duchowski, J. K.; Bocian, D. F. *J. Am. Chem. Soc.* **1988**, *110*, 6119.
(22) Lee, M.; Song, O.-K.; Seo, J.-C.; Kim, D.; Kim, H.-J.; Kim, K. *J. Phys. Chem.* **1992**, *96*, 8374.
(23) Deisenhofer, J.; Michel, H. *Science* **1989**, *245*, 1463.

Monomer   bisporphyrin

(D_{4h}) D_{4d}
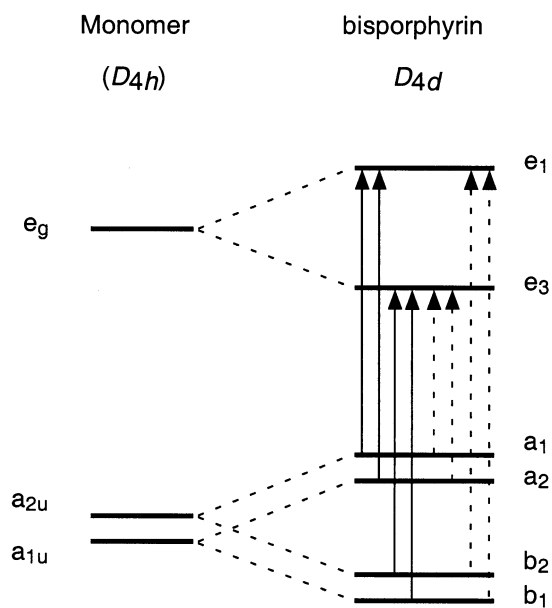
Figure 1. Schematic molecular orbital diagram of the supermolecule molecular orbitals (right side) formed from linear combinations of the four-orbital MOs (left side) of the constituent monoporphyrin complexes. The solid arrows denote the dipole-allowed (E_1) one-electron transitions and the dashed arrows are used for the dipole-forbidden (E_3) one-electron transitions.

between the two rings. Contrary to the Q′ and Q″ bands, the monomer-like Q and B bands are rather metal insensitive.[4] The main features of the electronic spectra of bis(porphyrin) complexes were originally interpreted in terms of relatively simple molecular orbital (MO) schemes.[21,24,25] A supermolecule MO plus configuration interaction (CI) model that readily explains the steady and the time-resolved electronic spectra of these systems was then proposed by Holten et al.[3,4] According to this model, the excited states are described as linear combinations (CI) of the excited configurations obtained by considering electron transitions from occupied to unoccupied supermolecule MOs which are formed by taking bonding and antibonding linear combinations of the monomer a_{1u} (π) and a_{2u} (π) HOMOs and e_g (π^*) LUMOs of the Gouterman four-orbital model. One-electron promotion among the eight orbitals of the sandwich (see Figure 1) results in four E_1 dipole-allowed and four E_3 dipole-forbidden excited-state configurations in the pertinent D_{4d} symmetry.

In the limit of degeneracy of the dipole-allowed configurations, (a_1e_1), (a_2e_1), (b_1e_3), and (b_2e_3), diagonalization of the CI matrix gives the singlet eigenfuntions B^+, Q^+, CR_1^+, and CR_2^+. The eigenfunctions B^+ and Q^+ are the allowed exciton states formed by in-phase combinations of the locally excited (intra-ligand) B and Q states of monomer subunits, and CR_1^+ and CR_2^+ are the allowed charge resonance (CR) states formed by in-phase combinations of the inter-ligand charge-transfer configurations. These wave functions provide a good description of the optical properties of the porphyrin double deckers. The pure exciton B^+ and Q^+ states account indeed for the nearly unperturbed (with respect to the monoporphyrin) B and Q bands, whereas the CR^+ states account for the new Q″ band. The CR character of the Q″ band is consistent with the observed

sensitivity of the energy and intensity of this band to the ionic radius of the metal ion, i.e., to the macrocycle separation. The four dipole-forbidden E_3 states have essentially mixed exciton and CR character. The lowest in energy which is largely derived from the (a_1e_3) and (a_2e_3) configurations is associated with the low-energy Q′ absorption.

It is the aim of this paper to provide the first accurate description of the excited states of zirconium(IV), cerium(IV), and thorium(IV) bis(octaethylporphyrin) complexes, using time-dependent density functional theory (TDDFT). TDDFT provides a first principles theory, which only recently has enabled the study of excitation energies, oscillator strengths, and (nonlinear) polarizabilities of systems of such size. TDDFT usually provides an accuracy for excitation energies that far exceeds that of the CI singles method, and which is often comparable in accuracy to the most advanced of the other ab initio approaches.[26−32] The reliability of the TDDFT approach in obtaining accurate predictions of excitation energies and oscillator strengths for metallotetrapyrroles is by now well-documented.[27,31,33−35] For a number of monoporphyrin and porphyrazine complexes, an extensive discussion on the performance of different exchange correlation potentials, such as the recent model Kohn−Sham (KS) potential, which is constructed with a statistical average of different model potentials for occupied KS orbitals (SAOP),[36,37] the standard generalized gradient approximated (GGA) potentials by Becke[38] (for exchange) and Perdew[39] (for correlation) and hybrid functionals (B3LYP)[40−43] has been reported in ref 32 .

In this paper we will focus on the bis(porphyrin) sandwiches of zirconium(IV), cerium(IV), and thorium(IV) because they provide an ideal series of molecules for studying the effects of the valence shell structure of the metal, of the size of the metal ion, and hence of the ring−ring separation on the ground- and excited-state properties of bis(porphyrins). In this series the mean separation between the nitrogen planes of the two porphyrin subunits varies indeed from ∼2.6 Å for Zr to ∼2.8 Å for Ce to ∼2.9 Å for Th, with a mean separation between the core atoms of the two π systems varying correspondingly from 3.2 to 3.5 Å. On going from Zr to Ce and Th, f orbitals come into play, which are expected to modify the valence molecular orbital pattern of the corresponding bis(porphyrinates) as well as the

(24) Duchowski, J. K.; Bocian, D. F. *J. Am. Chem. Soc.* **1990**, *112*, 3312.
(25) Perng, J.-H.; Duchowski, J. K.; Bocian, D. F. *J. Phys. Chem.* **1990**, *94*, 6684.

(26) van Gisbergen, S. J. A.; Rosa, A.; Ricciardi, G.; Baerends, E. J. *J. Chem. Phys.* **1999**, *111*, 2505.
(27) Sundholm, D. *Chem. Phys. Lett.* **1999**, *302*, 480.
(28) Sundholm, D. *Phys. Chem. Chem. Phys.* **2000**, *2*, 2275.
(29) van Gisbergen, S. J. A.; Groeneveld, J. A.; Rosa, A.; Snijders, J. G.; Baerends, E. J. *J. Phys. Chem. A* **1999**, *103*, 6835.
(30) Rosa, A.; Baerends, E. J.; van Gisbergen, S. J. A.; van Lenthe, E.; Groeneveld, J. A.; Snijders, J. G. *J. Am. Chem. Soc.* **1999**, *121*, 10356.
(31) Nguyen, K. A.; Pachter, R. *J. Chem. Phys.* **2001**, *114*, 10757.
(32) Baerends, E. J.; Ricciardi, G.; Rosa, A.; van Gisbergen, S. J. A. *Coord. Chem. Rev.* **2002**, *230*, 5.
(33) Ricciardi, G.; Rosa, A.; van Gisbergen, S. J. A.; Baerends, E. J. *J. Phys. Chem. A* **2000**, *104*, 635.
(34) Ricciardi, G.; Rosa, A.; Baerends, E. J. *J. Phys. Chem. A* **2001**, *105*, 5242.
(35) Rosa, A.; Ricciardi, G.; Baerends, E. J.; van Gisbergen, S. J. A. *J. Phys. Chem. A* **2001**, *105*, 3311.
(36) Gritsenko, O. V.; Schipper, P. R. T.; Baerends, E. J. *Chem. Phys. Lett.* **1999**, *302*, 199.
(37) Schipper, P. R. T.; Gritsenko, O. V.; van Gisbergen, S. J. A.; Baerends, E. J. *J. Chem. Phys.* **2000**, *112*, 1344.
(38) Becke, A. *Phys. Rev. A* **1988**, *38*, 3098.
(39) Perdew, J. P. *Phys. Rev. B* **1986**, *33*, 8822 (Erratum: Perdew, J. P. *Phys. Rev. B* **1986**, *34*, 7406).
(40) Becke, A. D. *J. Chem. Phys.* **1993**, *98*, 5648.
(41) Slater, J. C. *Quantum Theory of Molecules and Solids*; McGraw-Hill: New York, 1974; Vol. 4.
(42) Becke, A. D. *J. Chem. Phys.* **1988**, *88*, 1053.
(43) Lee, C.; Yang, W.; Parr, R. G. *Phys. Rev. B* **1988**, *37*, 785.

metal−ligand interactions. The presence of low-lying f orbitals in Ce is thought for instance to be responsible for cerium(IV) bis(porphyrinates) to manifest within the series peculiar electrochemical,[21] optical,[8] and photophysical[2,17] properties. The first reduction of sandwich complexes of Ce(IV) with OEP (OEP = octaethylporphyrin) and TPP (TPP = tetraphenylporphyrin) is extremely anodic compared with the first (porphyrin-centered) reduction of Zr(IV)[19] and Th(IV)[18] analogues, indicating that in Ce(IV) complexes it involves an orbital which is primarily metal in character. The optical spectra of cerium(IV) bis-(porphyrin) sandwiches show a weak broad absorption to the red of the Q band extending to about 2000 nm (0.62 eV),[8] a feature not shown by Zr(IV) and Th(IV) analogues, and associated with low-lying ring to metal charge-transfer (RMCT) states.[2,17] These are believed to play a crucial role in the ultrafast deactivation of the photoexcited cerium(IV) bis(porphyrin) sandwiches, which are, unlike the zirconium and thorium analogues, nonluminescent. [17]

Since the observed differences in the chemical and physical properties along the series rely primarily on the changes in the ground-state electronic structure, before dealing with the excited states, we will discuss in detail the ground-state electronic structure of these complexes with a special emphasis on the metal−ligand and ligand−ligand interactions. There are unanswered questions concerning the bond in this type of molecules, such as the following: (i) what is the interplay of metal−ligand and ligand−ligand interactions; (ii) how ionic or covalent are the metal−ligand interactions; (iii) what is in the lanthanide and actinide bis(porphyrin) complexes of the series the interplay of d and f orbitals in the metal−ligand bond?

To analyze the bond in the title sandwiches, we make extensive use of an energy decomposition scheme (see next section) that, combined with a fragment formalism, has proven to be a useful tool in the analysis of the bonding mechanisms in other porphyrin-like compounds.[44−46] For the heavier member of the series for which relativistic effects are relevant we make use of a combined scalar relativistic (SR) ZORA (zero-order regular approximation)[47−51] and DFT/TDDFT approach.

2. Method and Computational Details

The computational method we use is based on the time-dependent extension of density functional theory.[52−54] TDDFT is thoroughly reviewed in refs 52, 53, 55, and 56. In our implementation[54,57] the

solution of the TDDFT response equations proceeds in an iterative fashion starting from the usual ground-state or zero-order KS equations.[57] For these one needs an approximation to the usual static exchange-correlation (xc) potential $v_{xc}(\mathbf{r})$. After the ordinary KS equations have been solved, the first-order density change has to be calculated from an iterative solution to the first-order KS equations. In these first-order equations an approximation is needed to the first functional derivative of the time-dependent xc potential $v_{xc}(\mathbf{r},t)$ with respect to the time-dependent density $\rho(\mathbf{r}',t')$, the so-called xc kernel. For the xc kernel we use the Adiabatic Local Density Approximation (ALDA). In this approximation the time dependence (or frequency dependence if one talks about the Fourier transformed kernel) is neglected, and one simply uses the differentiated static LDA expression. In our case we use the Vosko−Wilk−Nusair parametrization.[58]

For the exchange-correlation potentials which appear in the zero-order KS equations we have used the GGA potential v^{BP}_{xc}, employing Becke's[38] gradient approximation for exchange and Perdew's[39] for correlation. Ground- and excited-state calculations have also been performed using the recent model KS exchange correlation potential v^{SAOP}_{xc}, which is constructed with a statistical average of different model potentials for occupied KS orbitals (SAOP).[36,37] Specifically, the potential may be written as a sum of model potentials v^{mod}_i, which are each strongly weighted in a region where an orbital density $\rho_i(\mathbf{r}) = n_i|\varphi_i(\mathbf{r})|^2$ dominates:

$$v_{xc}^{SAOP}(\mathbf{r}) = \sum_i^{occ} \frac{\rho_i(\mathbf{r})}{\rho(\mathbf{r})} v_i^{mod}(\mathbf{r})$$

The model potentials v_i^{mod} have the form

$$v_i^{mod}(\mathbf{r}) = a_i v^{Lba}_{xc}(\mathbf{r}) + (1 - a_i)v^{GLLB}_{xc}(\mathbf{r});$$
$$a_i = \exp[-2(\epsilon_{HOMO} - \epsilon_i)^2]$$

The v^{mod}_i asymptotically have the required $-1/r$ behavior (which the LDA and GGA potentials lack) since they acquire asymptotically the form of the LBA potential,[59] which has this behavior. In the inner region, notably in the atomic inner shells, the GLLB potential[60] dominates which approximates the shape of the exact Kohn−Sham potential with proper steplike behavior when going from one shell to the next inner shell. This step behavior is lacking in the LDA and GGA potentials. The SAOP potential thus by construction provides a balanced description of the electron exchange and correlation in both outer and inner atomic and molecular regions. High-quality results for a wide variety of response properties of prototype molecules have been obtained using v^{SAOP}_{xc}.[37] More recently this potential has been successfully used in ground- and excited-state calculations of transition metal tetrapyrroles.[32,34,35] SAOP results, not reported here, are generally very similar to BP results, except for the RMCT states, as a consequence of the upshift of the metal f levels and the downward shift of the metal d levels observed at the SAOP level. Relevant examples of the differences between BP and SAOP results will be given in the following.

The excitation energies of cerium and thorium bis(porphyrin) sandwiches are calculated by a combined scalar relativistic (SR) ZORA (zero-order regular approximation) and TDDFT approach which implies that the one-electron energies and the Kohn−Sham orbitals to be used in the TDDFT response equations are obtained by solving the one-electron (SR) ZORA Kohn−Sham equations.[50,51]

The calculations have been performed for the symmetry and spin allowed $^1B_2$ and $^1E_1$ states up to 3.5 eV, for the lowest symmetry forbidden $^1E_3$ states, and for the lowest symmetry allowed $^3E_1$ and $^3E_3$ triplet states.

(44) Rosa, A.; Baerends, E. J. *Inorg. Chem.* **1992**, *31*, 4717.
(45) Rosa, A.; Baerends, E. J. *Inorg. Chem.* **1994**, *33*, 584.
(46) Ricciardi, G.; Rosa, A.; Ciofini, I.; Bencini, A. *Inorg. Chem.* **1999**, *38*, 1422, and references therein.
(47) Chang, C.; Pelissier, M.; Durand, P. *Phys. Scr.* **1986**, *34*, 394.
(48) Heully, J.-L.; Lindgren, I.; Lindroth, E.; Lundqvist, S.; Màrtensson-Pendrill, A.-M. *J. Phys. B* **1986**, *19*, 2799.
(49) van Lenthe, E.; Baerends, E. J.; Snijders, J. G. *J. Chem. Phys.* **1993**, *99*, 4597.
(50) van Lenthe, E.; Baerends, E. J.; Snijders, J. G. *J. Chem. Phys.* **1994**, *101*, 9783.
(51) van Lenthe, E.; Ehlers, A. W.; Baerends, E. J. *J. Chem. Phys.* **1999**, *110*, 8543.
(52) Casida, M. E.. In *Recent Advances in Density Functional Methods*; Chong, D. P., Ed.; World Scientific: Singapore, 1995; Vol. 1, pp 155.
(53) Gross, E. U. K.; Dobson, J. F.; Petersilka, M. Density Functional Theory. In *Density Functional Theory;* Nalewajski, R. F., Ed.; Topics in Current Chemistry; Springer: Heidelberg, Germany, 1996.
(54) van Gisbergen, S. J. A.; Snijders, J. G.; Baerends, E. J. *Comput. Phys. Commun.* **1999**, *118*, 119.
(55) Gross, E. K. U.; Kohn, W. *Adv. Quantum Chem.* **1990**, *21*, 255.
(56) Gross, E. K. U.; Ullrich, C. A.; Gossmann, U. J. Density Functional Theory of Time-Dependent Systems. *Density Functional Theory of Time-Dependent Systems*; NATO ASI Series B; Plenum: New York, 1995; Vol. 337, p 149.
(57) van Gisbergen, S. J. A.; Snijders, J. G.; Baerends, E. J. *J. Chem. Phys.* **1995**, *103*, 9347.
(58) Vosko, S. H.; Wilk, L.; Nusair, M. *Can. J. Phys.* **1980**, *58*, 1200.
(59) van Leeuwen, R.; Baerends, E. J. *Phys. Rev. A* **1994**, *49*, 2421.
(60) Gritsenko, O. V.; van Leeuwen, R.; van Lenthe, E.; Baerends, E. J. *Phys. Rev. A* **1995**, *51*, 1944.
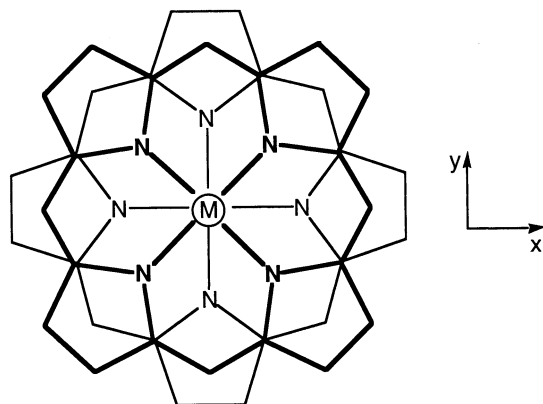
Figure 2. Configuration and orientation of the M(P)$_2$ (M = Zr, Ce, Th) bis(porphyrin) sandwiches.

All calculations reported in this paper have been performed with the parallelized ADF (Amsterdam density functional) suite of programs, release 2000.02.[61-63]

The calculations have been performed for the D_{4d} optimized geometries of the model systems M(P)$_2$ (M = Zr, Ce, Th; P = porphyrin). The orientation of the molecules is shown in Figure 2. To check for the effects of β-ethyl substituents on the electronic stucture and on the excited states, we have also performed calculations on Zr(OEP)$_2$ in the D_{4d} optimized geometry.

The (SR) ZORA geometries of Ce(P)$_2$ and Th(P)$_2$ were obtained using the recent implementation of analytical gradients for ZORA in ADF.[51] In the geometry optimizations the usual (nonrelativistic) BP density functional was used.

For the nonrelativistic calculations on Zr(P)$_2$ and on Zr(OEP)$_2$ we use the standard ADF V basis set,[64] which is an uncontracted triple-ζ STO basis set with one 3d and one 4f polarization function for the C and N atoms, one 2p and one 3d polarization function for H, and a triple-ζ nd, $(n + 1)$s basis with one $(n + 1)$p function for Zr. The cores (C, N, 1s; Zr, 1s–3d) were kept frozen. The all-electron ADF V basis set[64] was used in the SAOP calculations.

For the (SR) ZORA calculations on Ce(P)$_2$ and Th(P)$_2$ we use an optimized valence basis set[64] which is of the same size as the standard ADF V basis. It is an uncontracted triple-ζ STO 4f, 5d, and 6s basis with one 6p polarization function for Ce, and a triple-ζ 5f, 6d, and 7s basis with one 7p polarization function for Th. The cores (C, N, 1s; Ce, 1s–4d; Th, 1s–5d) are kept frozen and described by optimized (SR) ZORA orbitals. The all-electron ZORA-ADF V basis set[64] was used in the SAOP calculations.

To analyze the interaction between the metal and the (P)$_2$ cage, we decompose the interaction energy, ΔE_{int}, into a number of terms. The first term, ΔE^0, is obtained from the energy of the wave function Ψ^0 which is constructed as the antisymmetrized and renormalized product of the wave functions Ψ^A and Ψ^B of the fragments A and B (A = M; B = (P)$_2$):

$$\Psi^0 = NA\{\Psi^A\Psi^B\}$$

$$E^0 = \langle\Psi^0|H|\Psi^0\rangle, \quad E^A = \langle\Psi^A|H^A|\Psi^A\rangle, \quad E^B = \langle\Psi^B|H^B|\Psi^B\rangle$$

ΔE^0 is defined unambiguously as $\Delta E^0 = E^0 - E^A - E^B$. It consists of two terms, ΔE_{elstat} and ΔE_{Pauli}. The first term can be conceived as the classical electrostatic attraction between the unperturbed charge distributions of A and B; the second term originates from the Pauli antisymmetry principle and corresponds to the intuitive concept of steric

Chart 1

1a

1b
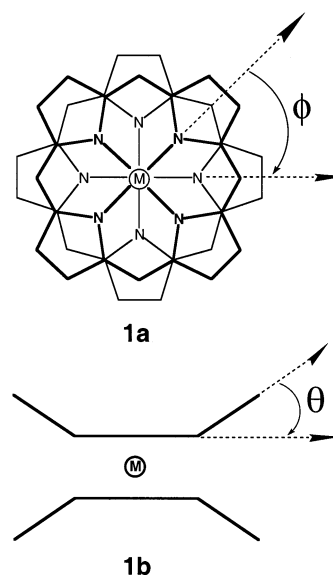
repulsion[65-67] that is widely used in chemistry. In addition to the ΔE^0 term, which is usually repulsive at the equilibrium distance since the repulsive component ΔE_{Pauli} dominates, there are the attractive orbital interactions, which enter when the wave function Ψ^0 is allowed to relax to the fully converged ground-state wave function of the overall molecule, Ψ^{AB}. The energy lowering due to mixing of virtual orbitals of the fragments into the occupied orbitals is called the electronic interaction energy, $\Delta E_{\text{oi}} = (\Psi^{AB}) - E^0$. This term, according to the decomposition scheme originally introduced by Ziegler and Rauk,[68] which is very useful for purposes of analysis, may be broken up into contributions from the orbital interactions within the various irreducible representations Γ of the overall symmetry group of the system:

$$\Delta E_{\text{int}} = \Delta E^0 + \Delta E_{\text{oi}} = \Delta E^0 + \Sigma_{\Gamma}\Delta E(\Gamma)$$

3. Ground-State Molecular and Electronic Structure of M(P)$_2$

(3a) Molecular Structure. The structural data available for Zr(OEP)$_2$,[12] Zr(TTP)$_2$,[11] Ce(OEP)$_2$,[69] and Th(TPP)$_2$[16] show that the bis(porphyrin) complexes of the investigated series share two relevant structural features: (i) the porphyrin rings adopt a staggered orientation (**1a**) with a staggering angle, ϕ, ranging from ~31° to ~44° that makes the coordination environment of each metal cation a slightly distorted square antiprism; (ii) both porphyrins are domed and severely distorted (**1b**), the average dihedral angles of the pyrrole rings, θ, ranging from ~15° to ~17° (Chart 1).

Staggering and doming of the tetrapyrrole rings are typical of all tetrapyrrole sandwich complexes, either homoleptic or heteroleptic. According to our quantitative energy analysis of the intra-dimer interactions in large- and small-ring metallotetrapyrrole based dimers,[44,70] and in metallodithiolene-type dimers,[71] both the staggering and the doming of the adjacent units are dictated by the necessity to minimize the steric hindrance

(61) Baerends, E. J.; Ellis, D. E.; Ros, P. *Chem. Phys.* **1973**, *2*, 41.
(62) te Velde, G.; Baerends, E. J. *J. Comput. Phys.* **1992**, *99*, 84.
(63) Fonseca Guerra, C.; Snijders, J. G.; te Velde, G.; Baerends, E. J. *Theor. Chem. Acc.* **1998**, *99*, 391.
(64) ADF "STO basis set database available on line at http://tc.chem.vu.nl/SCM/Doc/atomicdatabase,".

(65) Fujimoto, H.; Osamura, Y.; Minato, T. *J. Am. Chem. Soc.* **1978**, *100*, 2954.
(66) Kitaura, K.; Morokuma, K. *Int. J. Quantum Chem.* **1976**, *10*, 325.
(67) van den Hoek, P. J.; Kleyn, A. W.; Baerends, E. J. *Comments At. Mol. Phys.* **1989**, *23*, 93.
(68) Ziegler, T.; Rauk, A. *Theor. Chim. Acta* **1977**, *46*, 1.
(69) Buchler, J. W.; De Cian, A.; Fischer, J.; Kihn-Botulinski, M.; Paulus, H.; Weiss, R. *J. Am. Chem. Soc.* **1986**, *108*, 3652.
(70) Rosa, A.; Baerends, E. J. *Inorg. Chem.* **1993**, *32*, 5637.
(71) Rosa, A.; Ricciardi, G.; Baerends, E. J. *Inorg. Chem.* **1998**, *37*, 1368.

Table 1. Selected Average Bond Lengths (Å), Bond Angles (deg), and Metrical Parameters in Crystalline $Zr(OEP)_2$, $Zr(TPP)_2$, and $Ce(OEP)_2$, Compared with the Corresponding Theoretical, Optimized Values of $Zr(OEP)_2$ and the Model $M(P)_2$ (M = Zr, Ce, Th) Sandwich Complexes

param[a]	$Zr(P)_2$	$Zr(OEP)_2$[b]	$Zr(OEP)_2$[c]	$Zr(TPP)_2$[d]	$Ce(P)_2$	$Ce(OEP)_2$[e]	$Th(P)_2$
$M-N_{av}$[f]	2.418	2.420	2.383(9)	2.391(2)	2.525	2.475(1)	2.549 (2.55)[g]
$M-N_{center}$[h]	1.289	1.305	1.265	1.284	1.441	1.376	1.469 (1.47)[g]
θ (deg)	16	13	16	17	14	15	13
ϕ (deg)	45	45	44	37	45	42	45 (31)[g]
$N-C_\alpha$	1.379	1.378	1.378(5)	1.381(5)	1.376	1.375(1)	1.377
$C_\alpha-C_\beta$	1.442	1.423	1.442(9)	1.441(9)	1.445	1.449(1)	1.445
$C_\beta-C_\beta$	1.362	1.374	1.357(6)	1.334(5)	1.365	1.358(2)	1.366
$C_\alpha-C_b$	1.388	1.389	1.377(9)	1.394(7)	1.396	1.384(1)	1.398
$C_\alpha-N-C_\alpha$	104.9	105.0	104.3(5)	104.3(2)	106.1	105.6(1)	106.5
$N-C_\alpha-C_\beta$	110.9	111.2	111.3(5)	110.7(3)	110.0	110.4(1)	109.8
$C_\alpha-C_\beta-C_\beta$	106.6	106.2	106.4(4)	107.0(1)	106.8	106.7(1)	106.9
$C_\alpha-C_b-C_\alpha$	125.7	126.4	126.6(9)	123.2(5)	127.0	127.7(1)	127.5
$N-C_\alpha-C_b$	125.7	125.1	124.6(5)	126.4(8)	125.4	124.8(1)	125.3

[a] For the experimental data, the number in parentheses is the maximum deviation from the averaged value. [b] Optimized values, this work. [c] X-ray data from ref 12 [d] X-ray data from ref 11. [e] X-ray data from ref 69. [f] The experimental $M-N_{av}$ values represent the average distance from the metal to the eight coordinated pyrrolic nitrogens. The theoretical $M-N_{av}$ values indicate the distance from the metal to the eight pyrrolic nitrogens. [g] X-ray data for $Th(TPP)_2$ from ref 16. [h] $M-N_{center}$ represents the distance from the metal to the center-of-gravity for the eight coordinated pyrrolic nitrogens.

between the two macrocycles which the metal holds closer than their van der Waals distance and can be traced to Pauli repulsion between occupied orbitals.

In Table 1 the most relevant geometrical parameters calculated for the MP_2 (M = Zr, Ce, Th) model systems and for $Zr(OEP)_2$ are compared to the available X-ray data. According to Table 1, the bond lengths and angles calculated for the unsubstituted bisporphyrins are very close to those observed in OEP and TPP sandwiches, indicating that β-alkyl substitution and *meso*-phenyl substitution do not affect significantly the geometry of the porphyrin skeleton, which is consistent with the substantial invariance of bond lengths and angles in $Zr(OEP)_2$[12] and $Zr(TPP)_2$.[11] As inferred from Table 1, the metrical parameters, i.e., the staggering angle, ϕ, and the doming angle, θ, are on the contrary sensitive to the presence of the substituents, as well as to their nature and position. In particular, the measured inter-porphyrin twisting angles of 37° and 31° in $Zr(TPP)_2$ and $Th(TPP)_2$, respectively, and 44° and 42° in $Zr(OEP)_2$ and $Ce(OEP)_2$, respectively, clearly indicate that the OEP substituted sandwiches deviate very little from a D_{4d} conformation. Thus, our $M(P)_2$ models are suitable structural, and, as we will show later, also electronic, models for the octaethyl bis(porphyrin) sandwiches, but much less so for the tetraphenyl bis(porphyrin) sandwiches. When modeling $M(TPP)_2$ by $M(P)_2$, one would neglect the electronic structure changes of the porphyrin subunits induced by the *meso*-phenyl substituents, and, most importantly, one would not consider that going from the D_{4d} staggered conformation of $M(P)_2$ ($\phi = 45°$) to the D_4 staggered conformation ($\phi \neq 45°$) adopted by the $M(TPP)_2$ sandwiches, the overlap and the splitting of the frontier orbitals on adjacent porphyrin rings may change significantly. Therefore, retaining the full complexity of the TPP ring is crucial in interpreting the electronic and spectroscopic properties of the $M(TPP)_2$ sandwiches. A DFT/TDDFT investigation of the ground and excited states of $M(TPP)_2$ sandwiches will be published in a forthcoming paper.[72]

(3b) Level Schemes and Population Analyses. The highest occupied and lowest unoccupied one-electron levels for zirco-

(72) Ricciardi, G.; Rosa, A.; Baerends, E. J. Manuscript in preparation.

nium, cerium, and thorium bis(porphyrin) complexes are given in Figure 3, and for MOs with predominant ligand character the composition in terms of metal and $(P)_2$ fragment orbitals is given in Table 2.

In discussing the orbital composition of the $M(P)_2$ sandwiches, we will make use of the orbital interaction diagram of Figure 4, illustrating, for the representative case of $Th(P)_2$, the interactions between two P fragment orbitals (left side) in the $(P)_2$ cage and the interactions between $(P)_2$ and metal fragment orbitals (right side) in the thorium sandwich.

Of the P levels of Figure 4, $8b_1$ and $14e$ ("b_{1g}" and "e_u" in the D_{4h} ground-state symmetry of the bare porphyrin) are the N_p lone pairs of B_1 and E symmetry, respectively; the remaining are π orbitals. The origin and the spatial characteristics of the $P-\pi$ orbitals of Figure 4 have been recently highlighted by us using a fragment approach where four pyrrole rings and the methine bridges are taken as building blocks (see refs 32 and 35). According to our analysis, $9a_1$, $7b_1$, and $13e$ ("a_{2u}", "b_{2u}", and "e_g" in the D_{4h} ground-state symmetry of the bare macrocycle) belong to the e_x set of orbitals of the $(Py)_4$ cage and have a large amplitude at the pyrrolic nitrogens and (with opposite sign) at the C_β atoms, but no amplitude at the methine bridges. The Gouterman orbitals, $5a_2$ ("a_{1u}"), $10a_1$ ("a_{2u}"), and $15e$ ("e_g*") all derive from the e_y set of orbitals of the $(Py)_4$ cage, which, contrary to the e_x set, exhibit strong interaction with the methine bridges. However, while $15e$ is actually strongly delocalized on both the $(Py)_4$ and $(CH)_4$ fragments, $5a_2$ ("a_{1u}") and $10a_1$ ("a_{2u}") are not. These orbitals are also derived from the $(Py)_4$-e_y and π-CH orbitals, but, from the two orbitals, $1a_{1u}$ on the $(Py)_4$ and $1a_{2u}$ on $(CH)_4$ which find no partner on the other system and therefore end up in P as "nonbonding" orbitals at almost unchanged energies (see diagram of Figure 4 in ref 35).

As a matter of fact, $5a_2$ ("a_{1u}") has nodal planes through the CH bridges and is virtually a 100% $(Py)_4$-e_y orbital and $10a_1$ ("a_{2u}") is an in-phase combination of the π orbitals on the C atoms of the CH bridges with some admixture of the $3a_{2u}$ and $1a_{2u}$ $(Py)_4$ orbitals to the effect that it exhibits, in addition to a
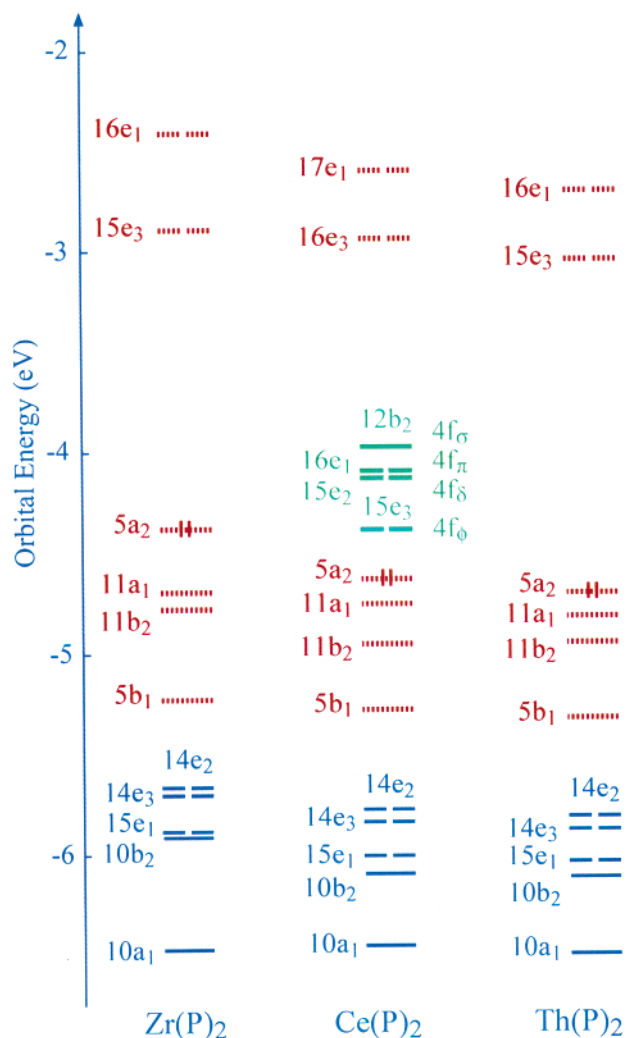
Figure 3. Energy level scheme for the M(P)$_2$ (M = Zr, Ce, Th) bis(porphyrin) sandwiches. Double occupancy is indicated for the HOMO only. All lower lying levels are also doubly occupied. The M(P)$_2$ MOs derived from the Gouterman's four orbitals of the constituent monoporphyrins are indicated with red hatched lines.

Table 2. Percentage Contribution of (P)$_2$ and M Fragments to Selected Orbitals (Based on Mulliken Population Analysis per MO) of M(P)$_2$ (M = Zr, Ce, Th)

		$-\epsilon$ (eV)	M	(P)$_2$
16(17)e$_1$	Zr(P)$_2$	2.42	0.0	96.0 (15e$_1$)
	Ce(P)2	2.60	0.0	96.0 (15e$_1$)
	Th(P)$_2$	2.67	1.0 (5f$_\pi$)	94.0 (15e$_1$)
15(16)e$_3$	Zr(P)$_2$	2.89	0.0	95.0 (15e$_3$)
	Ce(P)$_2$	2.97	0.0	95.0 (15e$_3$)
	Th(P)$_2$	3.03	0.0	94.0 (15e$_3$)
5a$_2$	Zr(P)$_2$	4.36		99.0 (5a$_2$)
	Ce(P)$_2$	4.64		99.0 (5a$_2$)
	Th(P)$_2$	4.69		99.0 (5a$_2$)
11a$_1$	Zr(P)$_2$	4.70	7.0 (4d$_\sigma$)	76.0 (10a$_1$); 13.0 (8a$_1$)
	Ce(P)$_2$	4.75	3.0 (5d$_\sigma$)	84.0 (10a$_1$); 11.0 (8a$_1$)
	Th(P)$_2$	4.81	3.0 (6d$_\sigma$)	81.0 (10a$_1$); 13.0 (8a$_1$)
11b$_2$	Zr(P)$_2$	4.79	1.5 (5p$_\sigma$)	90.0 (10b$_2$)
	Ce(P)$_2$	4.95	8.0 (4f$_\sigma$)	80.0 (10b$_2$)
	Th(P)$_2$	4.95	1.0 (5f$_\sigma$)	88.0 (10b$_2$)
5b$_1$	Zr(P)$_2$	5.22		99.0 (5b$_1$)
	Ce(P)$_2$	5.29		99.0 (5b$_1$)
	Th(P)$_2$	5.30		99.0 (5b$_1$)
14e$_2$	Zr(P)$_2$	5.67	0.0	76.0 (13e$_2$); 19.0 (14e$_2$)
	Ce(P)$_2$	5.78	1.0 (4f$_\delta$)	75.0 (13e$_2$); 20.0 (14e$_2$)
	Th(P)$_2$	5.81	0.0	75.0 (13e$_2$); 20.0 (14e$_2$)
14e$_3$	Zr(P)$_2$	5.69	0.0	92.0 (13e$_3$)
	Ce(P)$_2$	5.84	2.0 (4f$_\phi$)	90.0 (13e$_3$)
	Th(P)$_2$	5.87	0.0	90.0 (13e$_3$)
15e$_1$	Zr(P)$_2$	5.87	0.0	60.0 (13e$_1$); 35.0 (14e$_1$)
	Ce(P)$_2$	6.01	2.0 (4f$_\pi$)	67.0 (13e$_1$); 13.0 (14e$_1$)
	Th(P)$_2$	6.04	0.0	83.0 (13e$_1$); 8.0 (14e$_1$)
10b$_2$	Zr(P)$_2$	5.91	0.0	86.0 (9b$_2$); 14.0 (8, 10b$_2$)
	Ce(P)$_2$	6.10	2.0 (4f$_\sigma$)	89.0 (9b$_2$); 9.0 (8, 10b$_2$)
	Th(P)$_2$	6.13	0.0	89.0 (9b$_2$); 11.0 (8, 10b$_2$)
10a$_1$	Zr(P)$_2$	6.48	0.0	73.0 (9a$_1$); 27.0 (8, 10a$_1$)
	Ce(P)$_2$	6.46	3.0 (5d$_\sigma$)	77.0 (9a$_1$); 20.0 (8, 10a$_1$)
	Th(P)$_2$	6.50	4.0 (6d$_\sigma$)	94.0 (9a$_1$); 6.0 (8, 10a$_1$)

strong amplitude at the CH bridges, considerable amplitude with reversed sign at the N$_p$ (see plots of Figure 6 in ref 35).

Among the four highest occupied molecular orbitals of the M(P)$_2$ series depicted in Figure 3, 5a$_2$ (HOMO) and 5b$_1$ are the antibonding and bonding combinations, respectively, of the Gouterman 5a$_2$ ("a$_{1u}$") orbitals of the porphyrin rings. The quite large 5a$_2$/5b$_1$ energy gap in all systems is indicative of strong $\pi-\pi$ interaction between the 5a$_2$ π orbitals of the P subunits. This fits in with 5a$_2$ having large amplitude (more than 70%) on the C$_\alpha$ atoms (cf. ref 35), which at the staggering angle of 45° are eclipsed and well within the van der Waals contact. Due to the increasing separation between the two porphyrin subunits going from Zr to Ce and Th, the overlap integral of 5a$_2$, S(5a$_2$), decreases significantly along the series (0.086, 0.070, and 0.067 in Zr, Ce, and Th, respectively) to the effect that the 5a$_2$/5b$_1$ gap is in Zr(P)$_2$ larger than in Ce and Th analogues (0.87 eV vs 0.65 and 0.61 eV).

The 11a$_1$ and 11b$_2$ are bonding and antibonding combinations, respectively, of the Gouterman 10a$_1$ ("a$_{2u}$") orbitals of the two porphyrin rings. Due to the spatial characteristics of 10a$_1$, this orbital has indeed large amplitude on the pyrrolic nitrogens and

on the methine bridges (see discussion above), the overlap between the 10a$_1$ orbitals on adjacent rings is very small at the staggering angle of 45° and decreases dramatically with the increase of the inter-ring separation. The overlap integral of 10a$_1$ is only 0.017, 0.009, and 0.008 in Zr(P)$_2$, Ce(P)$_2$, and Th(P)$_2$, respectively. Therefore the 11a$_1$ and 11b$_2$ orbitals are better described as nonbonding MOs with respect to the ring−ring interaction.

The S(5a$_2$) and S(10a$_1$) values calculated for the M(P)$_2$ systems are perfectly in line with previous calculations by Rosa and Baerends on (NiP)$_2$ dimers at an inter-ring separation of ∼3.2 Å and at different staggering angles.[70] These calculations have shown indeed that the overlap between porphyrin a$_{1u}$ orbitals on adjacent rings changes from a positive large maximum at $\phi = 0°$ to an almost equally large negative minimum at $\phi = 45°$ and becomes 0 at $\phi \sim 20°$, whereas the overlap between porphyrin a$_{2u}$ orbitals on adjacent rings is largest, but still much smaller than the S(a$_{1u}$), near $\phi = 0°$ and decreases to a very small negative minimum as ϕ approaches 45°, becoming 0 at $\phi = 32°$ (cf. Figure 3 of ref 70).

As inferred from the level scheme of Figure 3, the antibonding combination of the P-10a$_1$ ("a$_{2u}$"), 11b$_2$, is invariably lower than its bonding counterpart, 11a$_1$. The 11a$_1$/11b$_2$ inversion is already operative in the (P)$_2$ cage (note the ordering of the parent 10a$_1$ and 10b$_2$ levels in the diagram of Figure 4) and is due to the mixing into these orbitals of the lower lying P-9a$_1$ and P-8a$_1$ derived orbitals (see the composition of 11a$_1$ and 11b$_2$ in Table 2) which destabilize both 11a$_1$ and 11b$_2$, but preferentially 11a$_1$. In the diagram of Figure 4 the stabilization of 11a$_1$ and 11b$_2$ of
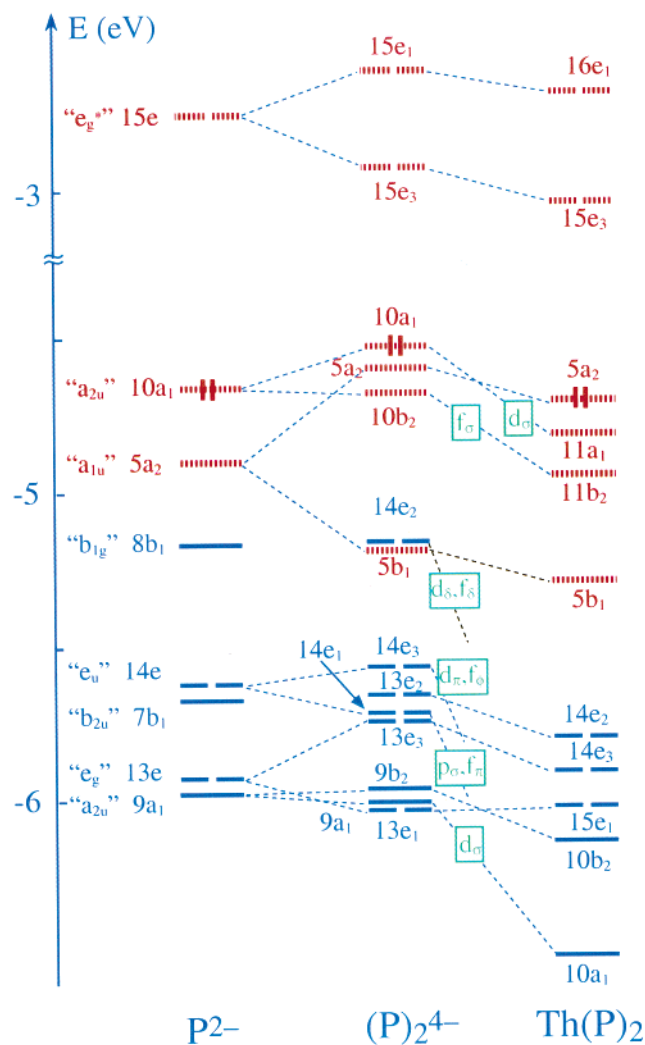
Figure 4. Orbital interaction diagram for interaction between two P^{2-} rings (left side) and for interaction between the $(P)_2^{4-}$ cage and Th^{4+}. The orbital levels of P^{2-} and $(P)_2^{4-}$ have been calculated for the neutral P and $(P)_2$ systems, respectively, but the orbital occupations refer to the closed shell P^{2-} and $(P)_2^{4-}$ species. The P levels have been rigidly shifted to higher energy by 0.43 eV to bring them into correspondence with unperturbed orbitals of the $(P)_2$ cage, and the $(P)_2$ levels have been rigidly shifted to higher energy by 0.18 eV to bring them into correspondence with pure $(P)_2$ MOs of the $Th(P)_2$ sandwich. Double occupancy is indicated for the HOMO only. All lower lying levels are also doubly occupied.

$Th(P)_2$ with respect to the parent $10a_1$ and $10b_2$ levels of the $(P)_2$ cage is also clearly distinguishable. The stabilization of $11a_1$ and $11b_2$ that occurs in all members of the series and is caused by a few percent admixture of metal orbitals (cf. Table 2) is not uniform, however, so that the $11a_1/11b_2$ gap does not conform to the decrease of the overlap integral going from Zr, to Ce and Th. The $11a_1$ is stabilized by d_σ orbitals in all systems, but especially in zirconium where we find 7% of the $4d_\sigma$ (we denote the orbitals on Zr, Ce, and Th by their linear symmetry labels); $11b_2$ is stabilized in thorium and especially in cerium by an admixture of f_σ orbitals, to the effect that the $11a_1/11b_2$ gap is largest in $Ce(P)_2$.

The important outcome of the quite different splitting of the P-$10a_1$ ("a_{2u}") and P-$5a_2$ ("a_{1u}") orbitals is that in all members of the $M(P)_2$ series the ordering of the highest four occupied orbitals differs significantly from that depicted in Figure 1, where similar splittings of the "a_{1u}" and "a_{2u}" orbitals are
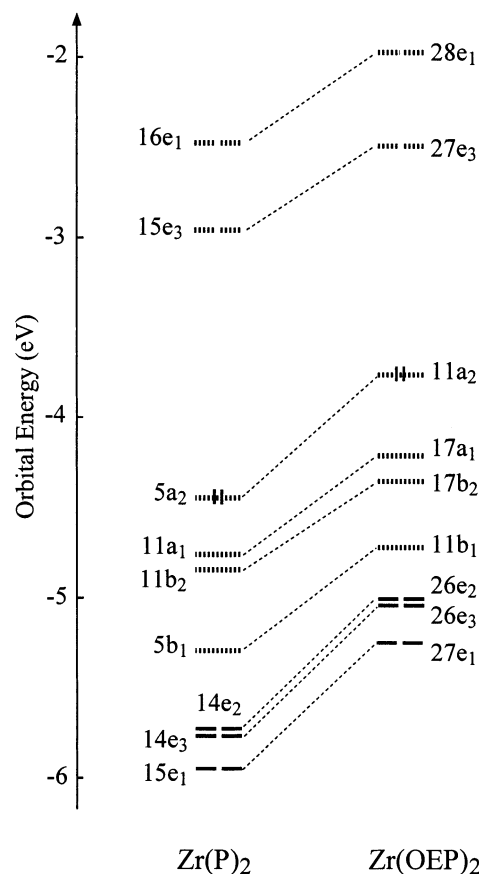
Figure 5. Energy level scheme for $Zr(P)_2$ and $Zr(OEP)_2$. Double occupancy is indicated for the HOMO only. All lower lying levels are also doubly occupied. The MOs of the bis(porphyrin) sandwiches derived from the Gouterman's four orbitals of the constituent monoporphyrins are indicated with hatched lines.

assumed. According to our results, $5b_1$ is well below ($\sim$0.4 eV) $11b_2$, whereas $5a_2$ and $11a_1$ are close in energy in Ce and Th, but not in Zr.

It is worth noting that the ordering of the four highest occupied levels hardly changes upon β-alkyl substitution of the P rings. Calculations performed on $Zr(OEP)_2$ in its optimized D_{4d} geometry show indeed that the pyrrolic β-ethyl groups only cause a nearly uniform upshift of $\sim$0.5 eV of the frontier orbitals (see Figure 5).

As inferred from the level scheme of Figure 3, a quite large ($\sim$0.5 eV) energy gap separates the a_{1u}- and a_{2u}-derived set of orbitals from the lower lying occupied orbitals. The $14e_2$, $14e_3$, $15e_1$, $10b_2$, and $10a_1$ are all derived from "e_x" type [35] (C_β,N_p π) P orbitals ($7b_1$, $13e$, and $9a_1$). Of these, $14e_2$ consist mainly of $13e_2$ of the $(P)_2$ cage. The two components of $(P)_2$-$13e_2$ are the + and − combinations of the $7b_1$ orbitals of the porphyrin rings (note that two b_1 orbitals in the local C_{4v} symmetry of the adjacent porphyrin rings have zero overlap due to the 45° rotation of the macrocycles, so they form + and − combinations that do not split in energy but constitute the two components of the e_2 set in the D_{4d} symmetry of the $(P)_2$ cage).

The $14e_3$ and $15e_1$ are composed primarily of $(P)_2$-$13e_3$ and $(P)_2$-$13e_1$, respectively, the higher lying $(P)_2$-$14e_3$ and $(P)_2$-$14e_1$ entering with only minor weight in their composition. The $10a_1$ and $10b_2$ are bonding and antibonding combinations, respectively, of the $9a_1$ ("a_{2u}") orbitals of the two porphyrin rings. The P-$9a_1$, just as the upper lying P-$10a_1$, split very little (see

the small energy gap between the $9b_2$ and $9a_1$ derived MOs of the P_2 cage in Figure 4). The large energy separation of the $10a_1$ and $10b_2$ MOs observed in the $M(P)_2$ systems is simply caused by the stabilization of the $10a_1$ by interaction with the d_σ metal orbital (cf. the composition of $10a_1$ in Table 2).

The orbitals with N_p lone pair character (P-$8b_1$ and P-$14e$) disappear from the $M(P)_2$ orbital spectrum. The higher lying $(P)_2$-$14e_2$ orbitals which are the degenerate $+$ and $-$ combinations of the P-$8b_1$ (N_p lone pair "b_{1g}") contribute only ∼20% to the composition of the $M(P)_2$-$14e_2$ MOs. The $(P)_2$-$14e_2$ orbitals, by virtue of their N_p lone pair character, are indeed strongly stabilized by interaction with d and f metal orbitals, d_π and f_δ in $Ce(P)_2$ and $Th(P)_2$ and d_π in $Zr(P)_2$, and are shifted below the energy range of Figures 3 and 4 (d_π denotes the d_{xz},d_{yz} pair; these have σ-type interaction with the N_p lone pairs to which their lobes point). Due to their N_p lone pair character, the $(P)_2$-$14e_3$ and $(P)_2$-$14e_1$ are, just as the $(P)_2$-$14e_2$, strongly stabilized by interaction with d_π, f_ϕ and p_π, f_π metal orbitals, respectively (see the interaction diagram of Figure 4). So all N_p lone pair combinations arising from the P-$8b_1$ and -$14e$ are shifted away by the interaction with the metal and will not affect the excitation spectrum in the Q, B band regions. The orbitals that remain below the set of four occupied Gouterman orbitals in the energy interval of interest are the "e_x" derived $14e_2$ (from P-$7b_1$), $14e_3$/$15e_1$ (from P-$13e$), and $10b_2$/$10a_1$ (from P-$9a_1$). Incidentally, $15e_1$ is ring−ring antibonding; $14e_3$, ring−ring bonding. This inversion, which already occurs in the $(P)_2$ system, is due to mixing in lower lying orbitals of $(P)_2$ (the same holds for the N_p lone pair derived set $14e_3$, $14e_1$ in $(P)_2$).

Coming now to the virtual orbitals, $15e_3$ and $16e_1$ ($16e_3$ and $17e_1$ in $Ce(P)_2$) are the bonding and antibonding combinations of the Gouterman $15e$ ("e_g*") orbitals of the porphyrin rings. The overlap between the P-$15e$ orbitals on adjacent rings decreases as the inter-ring separation increases along the series ($S(15e) = 0.046$, 0.037, and 0.036 in Zr, Ce, and Th, respectively). The energy gap between the bonding and antibonding combinations of the $15e$ follows the same trend as the overlap, being 0.46 eV in $Zr(P)_2$, 0.38 eV in $Ce(P)_2$, and 0.36 eV in $Th(P)_2$. As displayed in the level scheme of Figure 3, in $Ce(P)_2$, the $5a_2$-HOMO is separated from the Gouterman e_g*-derived $16e_3$/$17e_1$ bonding/antibonding pair by a set of virtual MOs which consist mainly of cerium 4f character. Of these MOs, $15e_3$, $15e_2$, and $16e_1$ are almost pure Ce(4f), $15e_2$ showing a few percent admixture of the occupied $14e_2$ orbital of the $(P)_2$ cage. The $12b_2$ is the antibonding combination of the Ce ($4f_\sigma$)−$(P)_2$ ($10b_2$) interaction. It is considerably mixed with a composition complementary to the bonding $Ce(P)_2$ $11b_2$ MO. Although the 4f orbitals of cerium do not mix strongly with occupied orbitals of the $(P)_2$ cage, considerable donation does take place into these orbitals (cf. the population of 4f orbitals reported in Table 3). It should be mentioned that DFT/SAOP calculations predict an upshift of the 4f set and a consequent increase of the HOMO−LUMO gap with respect to DFT/BP (1.08 vs 0.26 eV). As we will discuss later, due to the upshift of the 4f levels on going from BP to SAOP potential, the ring→4f RMCT states are computed at SAOP level at higher energies than at the BP level.

In $Th(P)_2$ the 5f set lies in the virtual spectrum in the region between -0.79 and -0.15 eV, well above the e_g*-derived $15e_3$/$16e_1$ bonding/antibonding pair. The composition of the corre-

Table 3. Analysis of the M−$(P)_2$ Bond in the $M(P)_2$ (M = Zr, Ce, Th) Complexes

		$Zr(P)_2$	$Ce(P)_2$	$Th(P)_2$
Bond Energy Decomposition (eV) in Terms of the Ionic Fragments M^{4+} and $(P)_2^{4-}$				
ΔE_{Pauli}		8.64	11.15	13.54
ΔE_{elstat}		-67.70	-67.07	-67.53
ΔE^0		-59.07	-55.92	-53.99
ΔE (A_1)		-6.31	-3.96	-4.43
ΔE (A_2)		-0.82	-0.77	-0.78
ΔE (B_1)		-0.84	-0.80	-0.82
ΔE (B_2)		-2.73	-4.71	-2.84
ΔE (E_1)		-7.52	-8.31	-7.28
ΔE (E_2)		-13.29	-12.83	-11.39
ΔE (E_3)		-14.65	-12.83	-11.90
ΔE_{oi}		-46.16	-44.21	-39.44
ΔE_{int}		-105.23	-100.13	-93.43
Fragment Orbital Population (Electrons)[a]				
	A_1			
M	$(n+1)$s	0.05	0.02	0.05
	nd_σ	0.25	0.12	0.15
$(P)_2$	Σ(virt)	0.07	0.04	0.05
	A_2			
$(P)_2$	Σ(virt)	0.02	0.02	0.02
	B_1			
$(P)_2$	Σ(virt)	0.01	0.01	0.02
	B_2			
M	$(n+1)p_\sigma$	0.00	0.00	0.00
	$(n-1)f_\sigma$		0.26	0.09
$(P)_2$	Σ(virt)	0.16	0.16	0.16
	E_1			
M	$(n+1)p_\pi$	0.00	0.04	0.00
	$(n-1)f_\pi$		0.24	0.18
$(P)_2$	Σ(virt)	0.14	0.16	0.16
	E_2			
M	nd_δ	0.62	0.54	0.66
	$(n-1)f_\delta$		0.36	0.30
$(P)_2$	Σ(virt)	0.14	0.16	0.16
	E_3			
M	nd_π	0.66	0.68	0.76
	$(n-1)f_\phi$		0.16	0.12
$(P)_2$	Σ(virt)	0.22	0.18	0.20

[a] Gross Mulliken population of M and $(P)_2$ fragment orbitals in the converged $M(P)_2$ sandwich complexes; $n = 4, 5, 6$ in Zr, Ce, and Th, respectively; all virtual $(P)_2$ orbitals of a given symmetry Γ are denoted by Σ(virt).

spondig MOs, $16e_2$, $16e_3$, $17e_1$, and $12b_2$, indicates that in thorium the 5f orbitals mix with occupied orbitals of the $(P)_2$ cage less than the 4f do in cerium and they acquire less charge than the Ce 4f (see Table 3).

As for the metal d states, they lie at very high energy in the virtual spectrum in all systems, in cerium and thorium well above the f states.

In $Zr(P)_2$ the lowest 4d state is $12a_1$ located at -1.71 eV which is a nearly pure (78%) Zr-$4d_{z^2}$(d_σ) metal orbital with a 15% antibonding admixture of the $10a_1$ orbital of the $(P)_2$ cage. The remaining 4d states lie at higher energy in the virtual spectrum since they are pushed up by strong interactions with the occupied orbitals of the $(P)_2$ cage. The $4d_{xy}$, $4d_{x^2-y^2}$ (d_δ) pair, which interacts with the $(P)_2$-$14e_2$, are found largely (more than 60%) in the $16e_2$ virtual MOs of $Zr(P)_2$. The d_{xz}, d_{yz} (d_π) pair is strongly destabilized by interaction with the $(P)_2$-$14e_3$. The populations of Zr-4d orbitals given in Table 3 confirm the strong interaction of occupied ring orbitals with the empty Zr-4d orbitals. In $Ce(P)_2$ and $Th(P)_2$, the d orbitals, especially d_δ and d_π, also show strong interactions with the just mentioned

occupied orbitals of the $(P)_2$ cage. The 5d are higher in energy than the 4f in Ce, and the 6d are higher than the 5f in Th; nevertheless they interact more effectively than the f orbitals, since they are spatially much more extended and overlap strongly with the low-lying orbitals of the $(P)_2$ cage. This is evident when comparing the populations of the d and f orbitals in the E_2 and E_3 symmetries.

(3c) Metal−$(P)_2$ Bonding Energies. A relevant point to arise from the electronic structure of $Zr(P)_2$, $Ce(P)_2$, and $Th(P)_2$ is that the $\pi-\pi$ interactions between the porphyrin subunits all consist of two-orbital four-electron destabilizing interactions, so the two macrocycles in the metal complexes are held together by the electrostatic interactions (M^{4+} with two P^{2-}) and the orbital interactions of occupied orbitals of the $(P)_2$ cage with empty metal orbitals.

The populations of the metal orbitals are a qualitative indication for the relative strengths of the metal−$(P)_2$ interactions, but not a quantitative measure of the corresponding energies. These are explicitly calculated according to the energy decomposition scheme and displayed in Table 3 for all members of the series.

To have clear and meaningful energy contributions in the individual irreducible representations, we promote the fragments to the ionic configurations $(P)_2^{4-}$ and M^{4+} (Zr, $(4d_\sigma)^0(4d_\pi)^0$-$(4d_\delta)^0(5s)^0$; Ce, $(4f_\sigma)^0(4f_\pi)^0(4f_\phi)^0(4f_\phi)^0(5d_\sigma)^0(5d_\pi)^0(5d_\delta)^0(6s)^0$; Th, $(5f_\sigma)^0(5f_\pi)^0(5f_\delta)^0(5f_\phi)^0(6d_\sigma)^0(6d_\pi)^0(6d_\delta)^0(7s)^0)$. Our analysis, using valence states of the fragments, refers to the final situation with the bonds formed. This change of configuration has the consequence that the Pauli repulsion due to 5s and 4d in the case of zirconium, 4f, 5d, and 6s in the case of cerium, and 6d and 7s in the case of thorium disappears.

As shown in Table 3, the ΔE^0 term is strongly attractive because the stabilizing contribution arising from the large attractive interaction between the charged fragments, ΔE_{elstat}, completely outweighs the positive, destabilizing Pauli repulsion term, ΔE_{Pauli}. While the ΔE_{elstat} term is almost constant along the series, the Pauli repulsion increases significantly as the number of closed shell electrons increases. Thus, the ΔE^0 term, which is the sum of ΔE_{elstat} and ΔE_{Pauli}, becomes somewhat less attractive on going from Zr to Ce and Th.

As far as the orbital interaction energies are concerned, we would stress that since we are considering ionic interacting fragments, it is expected that polarization of the $(P)_2^{4-}$ cage is important. The decomposition in energy contributions belonging to different irreducible representations does not distinguish charge transfer and polarization; however there are no metal orbitals that transform according to the A_2 and B_1 symmetries, and therefore the interaction energies in these "nonbonding" symmetries represent pure polarization arising from interaction between occupied and virtual orbitals of the $(P)_2^{4-}$ cage. The energetic effect of polarization (between 1.5 and 1.7 eV in these symmetries) is relatively small, but not negligible. We will also identify polarization contributions in other symmetries. As shown in Table 3, the $\Delta E(E_2)$ and $\Delta E(E_3)$ terms are by far the largest ones in all members of the series. These terms account for polarization of the cage (cf. the considerable amount of charge acquired by the empty $(P)_2$-e_2 and $(P)_2$-e_3 orbitals), for the interactions of occupied $(P)_2$ orbitals with d_δ and d_π and in the case of Ce and Th also with f_δ and f_ϕ orbitals. We note that the $\Delta E(E_2)$ and $\Delta E(E_3)$ terms decrease along the Zr, Ce, Th

series despite the comparable, in terms of transferred charge, polarization and donation into d_δ and d_π orbitals and of the additional charge donation into f_δ and f_ϕ orbitals in Ce and Th. The $\Delta E(E_2)$ and $\Delta E(E_3)$ trend suggests that the interactions of the $(P)_2^{4-}$ cage with the Zr $4d_{\delta,\pi}$ orbitals are energetically more important than those with Ce $5d_{\delta,\pi}$ and $4f_{\delta,\phi}$ orbitals and Th $6d_{\delta,\pi}$ and $5f_{\delta,\phi}$ orbitals. Polarization effects are important in the E_2 and E_3 symmetries, and although we cannot distinguish charge transfer and polarization in the $\Delta E(E_2)$ and $\Delta E(E_3)$ terms, nevertheless the −9.80 and −9.41 eV values computed for these tems in $Zr(P)_2$ with the Zr(4d) virtual orbitals deleted from the metal fragment Zr^{4+}, to prevent artificially any ring to metal 4d charge transfer, provide an indication of the large magnitude of the polarization contribution. The energetic contribution of polarization is also inferred from the large value of the $\Delta E(E_1)$ term in $Zr(P)_2$ (the largest term after $\Delta E(E_2)$ and $\Delta E(E_3)$ terms), where it accounts only for polarization effects. Polarization is actually even more important than charge transfer in the E_1 symmetry, as suggested by the modest change of the $\Delta E(E_1)$ term along the series, even though in Ce and Th this term additionally accounts for charge transfer into f_π orbitals and, in the case of $Ce(P)_2$, also into the $5p_\sigma$ orbitals. The $\Delta E(E_1)$ term decreases in fact by only 1.7 and 0.8 eV in $Ce(P)_2$ and $Th(P)_2$, respectively, when the virtual f orbitals are deleted from the metal fragments. As for the remaining two terms, the $\Delta E(A_1)$ and the $\Delta E(B_2)$, their contribution is less relevant than that of the $\Delta E(E_1)$, $\Delta E(E_2)$, and $\Delta E(E_3)$ terms, reflecting the smaller charge rearrangements occurring in A_1 and B_2 symmetries. The $\Delta E(A_1)$ term contains, apart from the contribution due to interaction of the occupied orbitals of the $(P)_2$ cage with d_σ and s orbitals, also a contribution due to polarization of the $(P)_2^{4-}$ cage. This term decreases significantly on going from Zr to Ce and Th, in line with the amount of the charge transfer to nd_σ observed in this symmetry. The $\Delta E(B_2)$ term is quite small in the zirconium and thorium sandwiches, where it exclusively or almost exclusively accounts for polarization, but increases by ∼2 eV in cerium because of the σ-donation into the $4f_\sigma$ orbital.

Finally we comment on the relative importance of ionic and covalent contributions to the bond in the $M(P)_2$ series. From the energy decomposition of Table 3 we find that the ΔE_{oi} term (covalent contribution) is stabilizing in all the investigated systems, being the largest in $Zr(P)_2$, but it is about 10% smaller than the $\Delta E°$ term which we may consider as a measure of the "ionic" contribution to the bonding. The total bonding energy $(\Delta E_{oi} + \Delta E°)$ indicates that the interaction between the $(P)_2^{4-}$ cage and the metal ions M^{4+} is strong in all members of the series but decreases on going from Zr to Ce and Th, due to the concomitant decrease of the covalent and ionic contributions, the latter caused by the increase of the Pauli repulsion.

4. Excited States and Optical Spectra

(4a) Q′ Band Region. As inferred from the ground-state absorption spectra of the $M(OEP)_2$ (M = Zr, Ce, Th) series displayed in Figures 6−8, the features of the weak broad red-region absorption, which is highly characteristic of bis(porphyrin) complexes, the Q′ band, change significantly on going from the transition metal to the lanthanide and actinide sandwich complexes. The solution spectrum of $Zr(OEP)_2$ shows a weak and broad Q′ absorption centered at lower energy (750 nm in dichloromethane[12]) than in $Ce(OEP)_2$ (640 nm in dichloromethane[21] and 647 nm in toluene[17]) and $Th(OEP)_2$ (710 nm
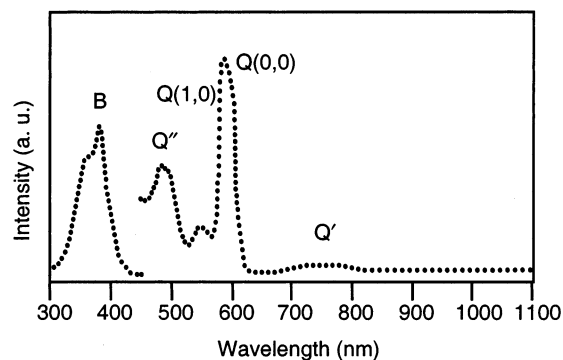
Figure 6. Absorption spectrum of Zr(OEP)$_2$ in dichloromethane at room temperature from ref 12.
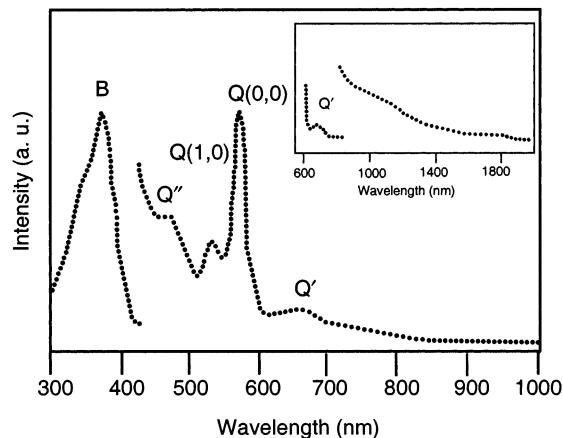
Figure 7. Absorption spectrum of Ce(OEP)$_2$ in dichloromethane at room temperature. UV−vis region from ref 17. (Inset) Near-IR region from ref 8.
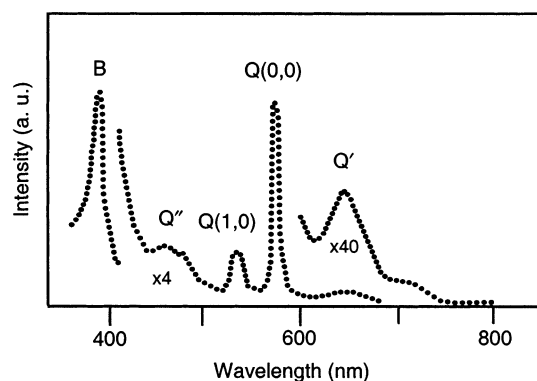
Figure 8. Absorption spectrum of Th(OEP)$_2$ in 3-methylpentane at 78 K from ref 4.

in toluene[1]). Additionally, the Q′ band region shows in Ce(OEP)$_2$ a broad tail extending into the near-infrared region up to ∼2000 nm (see inset of Figure 7) and in Th(OEP)$_2$ a second, more intense feature at 640 nm attributed to the ^{1}Q′ (1,0) vibronic transition.[4]

The excitation energies and oscillator strengths calculated for the lowest optically allowed ^{1}E$_1$ and ^{1}B$_2$ excited states and the excitation energies calculated for the lowest dipole forbidden ^{1}E$_3$ states of Zr(OEP)$_2$ and M(P)$_2$ (M = Zr, Ce, Th) model complexes are gathered in Tables 4−7 and compared with the experimental energy values determined from the solution spectra of the corresponding M(OEP)$_2$ sandwiches. Tables 4−7 also

include the compositions of the BP/ALDA solution vectors in terms of the major one-electron MO transitions.

We begin with Zr(P)$_2$ and Th(P)$_2$, and then we consider the case of Ce(P)$_2$, where the Q′ band region and its near-IR tail are complicated by the presence of RMCT states.

According to our TDDFT results the very weak Q′ band of Zr(OEP)$_2$ and Th(OEP)$_2$ is assigned to the dipole forbidden 1^{1}E$_3$ state computed for the corresponding model systems at 1.63 eV (761 nm) and 1.78 eV (697 nm), in excellent agreement with the experiment. Because the 1^{1}E$_3$ state in Zr(P)$_2$ and in Th(P)$_2$ is largely derived from the promotion of one electron from the antibonding 5a$_2$ (HOMO) to the bonding 15e$_3$ (LUMO), the potential energy curve of this state along the intermacrocycle distance coordinate is expected to be displaced to a shorter bond distance, relative to the ground state, leading to a shift of the Franck−Condon intensity from the origin to higher vibronic components and to a broad absorption contour.

The shift along the intermacrocycle distance coordinate predicted for the 1^{1}E$_3$ potential surface accounts very well for the observed breadth of the Q′ band and for the red shift (over 3000 cm^{-1}) relative to the ^{1}Q′ absorption maximum of the broad weak ^{1}Q′ fluorescence observed in zirconium, hafnium, and thorium bis(porphyrin) sandwiches.[1,3,4]

We predict a shift to longer wavelength of the 1^{1}E$_3$ state on going from Th(P)$_2$ to Zr(P)$_2$, as the splitting of the a$_{1u}$-derived 5a$_2$ increases (cf. the level scheme of Figure 3) due to the shortening of the intermacrocycle distance. This is in line with the observed red shift of the Q′ band on going from the actinide to the transition metal bis(porphyrin) sandwiches. The assignment of the Q′ band to a dipole forbidden E$_3$ state is also consistent with the weakness of this band.

The energy lowering by 0.19 eV of the Q′ state (l^{1}E$_3$) from Zr(P)$_2$ to Zr(OEP)$_2$ (see Table 4) can also be related to the increased splitting of the a$_{1u}$-derived 5a$_2$ orbital which is due, in this case, to minor changes of the composition of the a$_{1u}$ orbitals of the interacting monomers induced by the ethyl substituents.

In the energy regime of the Q′ band we compute in Zr(P)$_2$ and Th(P)$_2$ another dipole forbidden excited state, 2^{1}E$_3$, at 1.98 and 1.96 eV, respectively. This state, which is dominated by the 11a$_1$→15e$_3$ transition, contributes to the broadening of the Q′ band observed in the spectra of zirconium and thorium bis-(porphyrin) sandwiches. Although the energy of the 2^{1}E$_3$ state of Th(P)$_2$ is very close to the maximum of the absorption observed to the blue of the Q′ origin in the solution spectrum of Th(OEP)$_2$[4] (1.96 eV vs 1.93 eV), we think that this feature should be interpreted, according to the Bilsel et al.[4] suggestion, as the ^{1}Q′ (1,0) vibronic component of the ^{1}Q′ (0,0) transition. This feature is indeed absent in zirconium bis(porphyrin) sandwiches.

As far as the EX/CR character of the Q′ band is concerned, the model by Holten et al. predicts for the four dipole-forbidden ^{1}E$_3$ states, the lowest of which is associated with the low-energy Q′ absorption, a mixed exciton and charge resonance character.

We have also analyzed the Q′ state in terms of CR and EX contributions. To describe the excited states in terms of CR and EX contributions, we simply express the (approximate) wave function we obtain for a given excited state in terms of one electron transitions between occupied and unoccupied super-molecule (sandwich) MOs in terms of one electron transitions

Table 4. Calculated Excitation Energies (eV) and Oscillator Strengths (*f*) for the Optically Allowed $^1E_1$ and $^1B_2$ and for the Lowest Dipole Forbidden $^1E_3$ Excited States of Zr(P)$_2$ and Zr(OEP)$_2$ (in Parentheses) Compared to the Experimental Data[a]

state	composition (%)	excitation energy	f	assignment	expt Zr(OEP)$_2$
		Q′ Region			
1^1E_3	91 ($5a_2{\rightarrow}15e_3$)	1.63 (1.44)		Q′	1.65[b] (Q′)
	7 ($11a_1{\rightarrow}15e_3$)				
2^1E_3	81 ($11a_1{\rightarrow}15e_3$)	1.98 (1.90)			
	12 ($11b_2{\rightarrow}16e_1$)				
	5 ($5a_2{\rightarrow}15e_3$)				
		Q Region			
1^1E_1	63 ($11b_2{\rightarrow}15e_3$)	2.00 (1.91)	0.0011	Q tail	
	32 ($5a_2{\rightarrow}16e_1$)		(0.0279)		
2^1E_1	47 ($5a_2{\rightarrow}16e_1$)	2.10 (2.03)	0.0236	Q	2.09[b] (Q)
	18 ($5b_1{\rightarrow}15e_3$)		(0.0136)		
	18 ($11b_2{\rightarrow}15e_3$)				
	17 ($11a_1{\rightarrow}16e_1$)				
		Q″ Region			
3^1E_1	50 ($11a_1{\rightarrow}16e_1$)	2.39 (2.33)	0.0001	Q″	2.53[b] (Q″)
	45 ($5b_1{\rightarrow}15e_3$)		(0.0029)		
4^1E_1	97 ($14e_2{\rightarrow}15e_3$)	2.85 (2.56)	0.0058		
			(0.0036)		
		B Region			
5^1E_1	74 ($10b_2{\rightarrow}15e_3$)	3.00	0.1505	B tail	
	10 ($5b_1{\rightarrow}15e_3$)	(2.74)	(0.094)		
1^1B_2	70 ($15e_1{\rightarrow}15e_3$)	3.05	0.0081		
	23 ($11b_2{\rightarrow}12a_1$)				
2^1B_2	75 ($11b_2{\rightarrow}12a_1$)	3.20	0.0645		
	18 ($15e_1{\rightarrow}15e_3$)				
6^1E_1	97 ($14e_2{\rightarrow}16e_1$)	3.35	0.0034		
		(3.10)	(0.030)		
7^1E_1	23 ($10b_2{\rightarrow}15e_3$)	3.39	1.5338	B	3.24[b] (B)
	20 ($5b_1{\rightarrow}15e_3$)	(3.28)	(1.9214)		
	17 ($11a_1{\rightarrow}16e_1$)				
	11 ($5a_2{\rightarrow}16e_1$)				
	11 ($15e_1{\rightarrow}12a_1$)				
	9 ($11b_2{\rightarrow}15e_3$)				

[a] The major one-electron transitions contributing to the BP/ALDA solution vectors are also given for Zr(P)$_2$; the composition of the excited states of Zr(OEP)$_2$ is very similar except in the few cases explicitly discussed in the text. Gouterman orbitals are printed in italics. [b] Data taken from dichloromethane solution.[12]

between occupied and unoccupied fragment (monomer) MOs by decomposing the supermolecule MOs into linear combinations of fragment (monomer) MOs.

Our analysis confirms the mixed EX/CR character of the Q′ state suggested by Holten et al., as predicts for this state a roughly 50/50 EX/CR character in the case of zirconium and a 37/63 EX/CR character in the case of thorium.

However, looking in more detail at the composition of the lowest singlet E$_3$ states, it is apparent that the suggestion by Holten et al, according to which in the four E$_3$ configurations the near-degeneracy within the a$_{1u}$- and a$_{2u}$-derived pairs of configurations (a$_1$e$_3$)/(a$_2$e$_3$) (short dashed arrows in Figure 1) and (b$_2$e$_1$)/(b$_1$e$_1$) (long dashed arrows in Figure 1) is preserved, is not confirmed by our calculations. The 5a$_2{\rightarrow}$15e$_3$ and 11a$_1{\rightarrow}$15e$_3$ transitions are found indeed to mix very little in the two lowest $^1E_3$ states, especially in the zirconium sandwich where the 11a$_1$/5a$_2$ gap is larger than in thorium; the same is for the 11b$_2{\rightarrow}$16e$_1$ and 5b$_1{\rightarrow}$16e$_1$ transitions which enter with a weight of 65 and 20%, respectively, in the composition of the 3$^1E_3$ computed at 2.58 eV in zirconium and at 2.50 eV in thorium and with a reversed weight in the 5$^1E_3$ computed at 3.14 eV in zirconium and at 3.08 eV in thorium.

Coming now to Ce(P)$_2$, dipole forbidden $^1E_3$ and weak dipole allowed $^1B_2$ and $^1E_1$ RMCT excited states are calculated in the near-IR region (see Table 6). They are responsible for the weak absorption to the red of the Q′ band extending to about 2000 nm into the near-IR. According to their composition, these RMCT states have a monotransition character and involve transitions to the cerium 4f set of orbitals. It is just because of their ring→4f character that these RMCT states are predicted at the SAOP level at energies considerably higher than at the BP level of theory (compare BP and SAOP excitation energies of Table 6). As a consequence, of the RMCT states gathered in Table 6, only the lowest seven are predicted at the SAOP level in the near-IR region, the remaining contributing to the region of the Q bands.

As inferred from Table 7, the transition from the antibonding 5a$_2$ (HOMO) to the bonding e$_g$* derived 16e$_3$ MO, which almost entirely accounts for the 1$^1E_3$ Q′ state in Zr(P)$_2$ and Th(P)$_2$, in Ce(P)$_2$ strongly mixes with the close-lying 14e$_3{\rightarrow}$15e$_2$ RMCT transition. Two nearly degenerate excited states result, the dipole forbidden 7$^1E_3$ and 8$^1E_3$ calculated at 1.78 and 1.79 eV, respectively. In the Q′ band region we also compute three dipole

Table 5. Calculated Excitation Energies (eV) and Oscillator Strengths (f) for the Optically Allowed $^1E_1$ and $^1B_2$ and for the Lowest Dipole Forbidden $^1E_3$ Excited States of Th(P)$_2$ Compared to the Experimental Data[a]

state	composition (%)	excitation energy	f	assignment	expt Th(OEP)$_2$
		Q′ Band Region			
1^1E_3	74 (*5a₂→15e₃*)	1.78		Q′	~1.74[b] (Q′)
	26 (*11a₁→15e₃*)				
2^1E_3	61 (*11a₁→15e₃*)	1.96			
	17 (*11b₂→16e₁*)				
	18 (*5a₂→15e₃*)				
		Q Band Region			
1^1E_1	70 (*11b₂→15e₃*)	2.00	0.0004	Q tail	
	23 (*11a₁→16e₁*)				
2^1E_1	69 (*5a₂→16e₁*)	2.11	0.0083	Q	2.15;[b] 2.14[c] (Q)
	22 (*5b₁→15e₃*)				
	9 (*11a₁→16e₁*)				
		Q″ Band Region			
3^1E_1	46 (*5b₁→15e₃*)	2.31	0.0002	Q₁″	~2.6[d] (Q₁″); 2.63 (sh)[c] (Q″)
	40 (*11a₁→16e₁*)				
	9 (*11b₂→15e₃*)				
4^1E_1	93 (*14e₂→15e₃*)	2.83	0.0052	Q₂″	~2.7[d] (Q₂″)
		B Band Region			
1^1B_2	83 (*15e₁→15e₃*)	3.08	0.0020	B tail	
	16 (*14e₃→16e₁*)				
5^1E_1	75 (*10b₂→15e₃*)	3.08	0.1955		
	8 (*5b₁→15e₃*)				
6^1E_1	91 (*14e₂→16e₁*)	3.21	0.0053		
2^1B_2	82 (*14e₃→16e₁*)	3.35	0.0192		
	15 (*15e₁→15e₃*)				
7^1E_1	19 (*10b₂→15e₃*)	3.52	2.002	B	3.24;[b] 3.23[c] (B)
	19 (*5b₁→15e₃*)				
	16 (*11a₁→16e₁*)				
	13 (*5a₂→16e₁*)				
	11 (*11b₂→15e₃*)				

[a] The major one-electron transitions contributing to the BP/ALDA soluction vectors are also given; Gouterman orbitals are printed in italics. [b] Data taken from toluene solution.[1] [c] Data taken from 3-methylpentane solution.[18] [d] Data taken from 3-methylpentane glass at 78 K.[4]

Table 6. Calculated Excitation Energies (eV) and Oscillator Strengths (f) for the Optically Allowed $^1E_1$ and $^1B_2$ and for the Dipole Forbidden $^1E_3$ Excited States of Ce(P)$_2$ Contributing to the Near-IR Region of Ce(OEP)$_2$[a,b]

state	composition (%)	excitation energy	f	expt[c] Ce(OEP)$_2$
1^1E_3	100 (*5a₂→15e₃*)	0.26 (1.09)		
2^1E_3	100 (*11a₁→15e₃*)	0.37 (1.26)		
1^1E_1	100 (*5a₂→16e₁*)	0.57 (1.26)	0.0003	
2^1E_1	100 (*11b₂→15e₃*)	0.58 (1.43)	0.0001	
3^1E_1	99 (*11a₁→16e₁*)	0.68 (1.44)	0.0002	
1^1B_2	99 (*11a₁→12b₂*)	0.83 (1.39)	0.0041	
3^1E_3	99 (*11b₂→16e₁*)	0.85 (1.59)		
4^1E_1	99 (*5b₁→15e₃*)	0.91 (1.69)	0.0006	
4^1E_3	99 (*5b₁→16e₁*)	1.21 (1.87)		0.70−1.75 eV
5^1E_1	99 (*14e₂→15e₃*)	1.39 (2.32)	0.0011	near-IR tail
5^1E_3	99 (*14e₂→15e₃*)	1.41 (2.34)		
2^1B_2	92 (*15e₁→15e₃*)	1.64 (2.55)	0.0035	
6^1E_1	84 (*14e₂→16e₁*)	1.70 (2.50)	0.0008	
3^1B_2	78 (*14e₂→15e₂*)	1.71 (2.54)	0.0013	
6^1E_3	93 (*14e₂→16e₁*)	1.71 (2.51)		
7^1E_1	85 (*10b₂→15e₃*)	1.73 (2.60)	0.0036	
8^1E_1	98 (*14e₃→15e₂*)	1.76 (2.59)	0.0005	

[a] The major one-electron transitions contributing to the BP/ALDA soluction vectors are also given; Gouterman orbitals are printed in italics. [b] SAOP/ALDA excitation energies are reported in parentheses. [c] Data taken from cyclohexane solution.[8]

allowed excited states, the moderately intense 4^1B_2 and the very weak 9^1E_1 and 10^1E_1, all having a predominant RMCT character.

It is worth mentioning that at the SAOP level the $5a_2→16e_3$ transition does not mix with the $14e_3→15e_2$ RMCT transition, due to the mentioned upshift of the ring→4f transitions. TDDFT/SAOP calculations predict indeed only two singlet E$_3$ excited states in the Q′ band region. The lower, at 1.78 eV, is largely described by the $5a_2→16e_3$ transition with only 10% contribution of the $5b_1→15e_3$ RMCT transition; the higher, at 1.87 eV, is an almost pure $5b_1→16e_1$ RMCT state.

The presence of a cascade of singlet RMCT excited states in the Q′ band region and in the near-IR, predicted both at BP and SAOP levels, nicely accounts for the rapid radiationless decay of Ce(OEP)$_2$ upon excitation with 582 nm flash[2] and strongly supports the suggestion by Holten et al.[2] that the ultrafast (1.5 ps) process following excitation of Ce(OEP)$_2$ is due to excited-state deactivation to the electronic ground state via low-lying RMCT states.

(4b) Q Band Region. The solution spectra of M(OEP)$_2$ (M = Zr, Ce, Th) show to the blue of the Q′ band Q(0,0) and Q(1,0) bands (cf. Figures 6−8) that have essentially the same position and intensity exhibited by the analogous mono(porphyrin) complexes. According to the computed excitation energies and oscillator strengths, the 2^1E_1 excited state computed for Zr(P)$_2$ and Th(P)$_2$ model sandwiches at 2.10 and 2.11 eV, respectively, is responsible for the Q(0,0) band observed in Zr(OEP)$_2$ at 2.09 eV and in Th(OEP)$_2$ at 2.14−2.15 eV, whereas the Q(0,0) band

Table 7. Calculated Excitation Energies (eV) and Oscillator Strengths (f) for the Optically Allowed $^1E_1$ and $^1B_2$ and for the Dipole Forbidden $^1E_3$ Excited States of Ce(P)$_2$ Contributing to the Q′, Q, Q″, and B Band Regions Compared to the Experimental Data[a]

state	composition (%)	excitation energy	f	assignment	expt Ce(OEP)$_2$
		Q′ Band Region			
7^1E_3	46 ($14e_3{\rightarrow}15e_2$)	1.78			
	38 (*$5a_2{\rightarrow}16e_3$*)				
8^1E_3	52 ($14e_3{\rightarrow}15e_2$)	1.79			
	30 (*$5a_2{\rightarrow}16e_3$*)				
4^1B_2	80 ($14e_3{\rightarrow}16e_1$)	1.83	0.0302	Q′	~1.87;[b] ~1.93[c]
	15 ($14e_2{\rightarrow}15e_2$)				(Q′)
9^1E_1	94 ($14e_3{\rightarrow}12b_2$)	1.90	0.0006		
10^1E_1	96 ($15e_1{\rightarrow}15e_2$)	1.94	0.0003		
		Q Band Region			
11^1E_1	70 (*$11b_2{\rightarrow}16e_3$*)	2.04	0.0001	Q tail	
	23 (*$11a_1{\rightarrow}17e_1$*)				
12^1E_1	70 (*$5a_2{\rightarrow}17e_1$*)	2.13	0.0112	Q	2.16b; 2.16[c]
	17 (*$5b_1{\rightarrow}16e_3$*)				(Q)
	13 (*$11a_1{\rightarrow}17e_1$*)				
		Q″ Band Region			
13^1E_1	48 (*$5b_1{\rightarrow}16e_3$*)	2.34	0.0007		
	39 (*$11a_1{\rightarrow}17e_1$*)				
	10 (*$11b_2{\rightarrow}16e_3$*)				
14^1E_1	99 ($10a_1{\rightarrow}16e_1$)	2.40	0.0008		
16^1E_1	93 ($13e_1{\rightarrow}15e_2$)	2.61	0.0072	Q″	2.65;[b] 2.65[c]
18^1E_1	98 ($9b_2{\rightarrow}15e_3$)	2.74	0.0022		(Q″)
19^1E_1	95 ($14e_2{\rightarrow}17e_1$)	2.85	0.0059		
		B Band Region			
20^1E_1	92 ($13e_2{\rightarrow}16e_1$)	2.94	0.0308	B tail	
21^1E_1	99 ($13e_3{\rightarrow}15e_2$)	3.01	0.0024		
22^1E_1	50 (*$11a_1{\rightarrow}16e_1$*)	3.11	0.1350		
	45 (*$5b_1{\rightarrow}15e_3$*)				
10^1B_2	76 ($15e_1{\rightarrow}16e_3$)	3.13	0.0011		
	16 ($14e_3{\rightarrow}17e_1$)				
23^1E_1	56 ($10b_2{\rightarrow}16e_3$)	3.16	0.0238		
	37 ($13e_3{\rightarrow}12b_2$)				
24^1E_1	94 ($14e_2{\rightarrow}17e_1$)	3.26	0.0179		
25^1E_1	98 ($12e_2{\rightarrow}15e_3$)	3.36	0.0122		
11^1B_2	82 ($14e_3{\rightarrow}17e_1$)	3.39	0.0175		
	14 ($15e_1{\rightarrow}16e_3$)				
26^1E_1	55 ($12e_3{\rightarrow}15e_2$)	3.50	0.5418	B	3.28;[b] 3.28[c]
	9 (*$10b_2{\rightarrow}16e_3$*)				(B)
	7 ($12e_3{\rightarrow}12b_2$)				
	7 (*$5b_1{\rightarrow}16e_3$*)				
	5 (*$11a_1{\rightarrow}17e_1$*)				
	5 (*$5a_2{\rightarrow}17e_1$*)				
	5 (*$11b_2{\rightarrow}16e_3$*)				

[a] The major one-electron transitions contributing to the BP/ALDA solution vectors are also given; Gouterman orbitals are printed in italics. [b] Data taken from cyclohexane solution.[69] [c] Data taken from dichloromethane solution.[21]

of Ce(OEP)$_2$ at 2.16 eV is very well accounted for by the 12^1E_1 excited state computed for Ce(P)$_2$ at 2.13 eV.

The composition of the BP/ALDA solution vectors in terms of the major one-electron MO transitions reveals that in Th(P)$_2$ and Ce(P)$_2$ the Q state is dominated (~70%) by the $5a_2{\rightarrow}16$-(17)e_1 transition, the $5b_1{\rightarrow}15(16)e_3$, and $11a_1{\rightarrow}16(17)e_1$ transitions entering with a minor weight, whereas in Zr(P)$_2$ it contains only a 47% contribution of the $5a_2{\rightarrow}16e_1$ transition, the

remaining 43% being equally divided among the other dipole allowed configurations involving the eight frontier orbitals.

Although the $\langle5a_2|x,y|16e_{1,y,x}\rangle$, $\langle5b_1|x,y|15e_{3,xz,yz}\rangle$, $\langle11a_1|x,y|16e_{1,x,y}\rangle$, and $\langle11b_2|x,y|15e_{3,yz,xz}\rangle$ dipole matrix elements are quite large (they amount in Zr(P)$_2$ to 3.33, 3.21, 2.98, and 2.70 au, respectively, and in Ce(P)$_2$ and Th(P)$_2$ they have nearly identical values), the oscillator strength of the Q state is so low because the phases of the mixing coefficients of the contributing transitions (three in the case of cerium and thorium, four in the case of zirconium) are such that their transition dipole moments combine destructively, a mechanism that, mutatis mutandis, is the same as the one leading in monoporphyrins to a very weak Q state.

The quite different weights with which the four E_1 configurations (a_2e_1), (a_1e_1), (b_1e_3), and (b_2e_3) enter in the composition of the Q state point to their nondegeneracy. That these configurations may not be degenerate, as assumed in the eight orbital model, might have been already argued from the ordering of the highest four occupied orbitals of the M(P)$_2$ model systems, which, as stressed in the previous section, differs significantly from that of the eight orbital model (compare Figure 3 and Figure 1). Due to the different splitting of the P-10a_1 and P-5a_2 orbitals (the P-5a_2 orbitals on adjacent rings overlap to a much larger extent than the P-10a_1 orbitals do), the near-degeneracy of the a_{1u}- and a_{2u}-derived bonding and antibonding pairs assumed in the eight orbital model and depicted in the scheme of Figure 1 is indeed partially lost.

The breakdown of the near-degeneracy of the four E_1 configurations involving the eight frontier orbitals of the bis(porphyrin) sandwiches also reflects on the EX/CR description of the Q-band for which we predict, at variance with the model by Holten et al.,[3,4] a predominant charge resonance character, according to the analysis of the pertinent excited state in terms of excitonic and charge resonance contributions in the following.

For one component of the degenerate 2^1E_1(Q) excited state of Zr(P)$_2$ the (approximate) wave function in terms of supermolecule (sandwich) MOs

$$\Psi(2^1E_1) = -0.68(5a_2{\rightarrow}16e_{1,y}) + 0.43(5b_1{\rightarrow}15e_{3,xz}) - 0.42(11b_2{\rightarrow}15e_{3,yz}) - 0.42(11a_1{\rightarrow}16e_{1,x}) + ...$$

is expanded in terms of intraligand, excitonic (A→A, B→B) and interligand, charge resonance (A→B, B→A) one-electron transitions by decomposing the supermolecule MOs into linear combinations of fragment (monomer) MOs

$$\Psi(2^1E_1) = +0.07(5a_2{}^A{\rightarrow}15e_{xz}{}^A) - 0.23(5a_2{}^A{\rightarrow}15e_{yz}{}^A) + 0.07(5a_2{}^B{\rightarrow}15e_{xz}{}^B) - 0.23(5a_2{}^B{\rightarrow}15e_{yz}{}^B) + 0.40(10a_1{}^B{\rightarrow}15e_{xz}{}^B) - 0.16(10a_1{}^B{\rightarrow}15e_{yz}{}^B) + 0.43(5a_2{}^A{\rightarrow}15e_{xz}{}^B) + 0.51(5a_2{}^A{\rightarrow}15e_{yz}{}^B) + 0.33(5a_2{}^B{\rightarrow}15e_{xz}{}^A) + 0.39(5a_2{}^B{\rightarrow}15e_{yz}{}^A) + 0.40(10a_1{}^B{\rightarrow}15e_{xz}{}^A) - 0.16(10a_1{}^B{\rightarrow}15e_{yz}{}^A) + ...$$

which affords a 70/30 CR/EX character for this state.

An analysis of the Q state of Ce(P)$_2$ and Th(P)$_2$ along these lines affords for this state 75/15 and 77/13 CR/EX character, respectively. Our calculations therefore do not confirm the suggestion that the Q state in these sandwiches is a linear combination of monomer Q states (i.e. has excitonic character).

We predict immediately to the red of the Q state another, weaker excited state, 1^1E_1 in $Zr(P)_2$ and $Th(P)_2$ and 11^1E_1 in $Ce(P)_2$, that contributes to the broadening of the Q(0,0) band, a feature clearly visible in the solution spectra of $Zr(OEP)_2$ and $Ce(OEP)_2$. This state is dominated in all sandwiches by the $11b_2 \rightarrow 15(16)e_3$ transition ("a_{2u}" to e_g* excitation), with a minor contribution of $5a_2 \rightarrow 16e_1$ in zirconium and of $11a_1 \rightarrow 16(17)e_1$ in cerium and thorium. Just as for the Q state, a mixed CR/EX character is predicted for the lower lying singlet E_1 state, for which we find a CR/EX character of 50/50, 47/53, and 51/49 in zirconium, cerium, and thorium, respectively.

Calculations on $Zr(OEP)_2$ show that the β-ethyl substituents have an almost negligible effect on the energy of the Q-band and of its red tail, more significant being the effect on the intensities. The increase of the oscillator strengths of the 1^1E_1 state, as well as the decrease of the oscillator strengths of the 2^1E_1 state in $Zr(OEP)_2$ are caused by the change in the composition of these states, in particular the weights of the $11b_2 \rightarrow 15e_3$ and $5a_2 \rightarrow 16e_1$ transitions in these states are reversed relative to $Zr(P)_2$.

(4c) Q″ Band Region. The solution spectra of $Zr(OEP)_2$, $Ce(OEP)_2$, and $Th(OEP)_2$ show to the blue of the Q bands a broad and weaker band denoted Q″. At least two weak features underlie the broad Q″ absorption which are clearly distinguishable in the low-temperature solution spectrum of $Th(OEP)_2$ (see Figure 8) and which we have denoted in Table 5 as $Q_1″$ and $Q_2″$.

Our calculations on the model $M(P)_2$ sandwiches predict in the Q″ region two ligand centered $^1E_1$ excited states (the 3^1E_1 and 4^1E_1 in $Zr(P)_2$ and $Th(P)_2$, the 13^1E_1 and 19^1E_1 in $Ce(P)_2$) and in the case of $Ce(P)_2$ also several RMCT $^1E_1$ and $^1B_2$ excited states.

The $Q_1″$ and $Q_2″$ features appearing in the low-temperature spectrum of $Th(OEP)_2$ at ∼2.6 and ∼2.7 eV are satisfactorily accounted for by the 3^1E_1 and 4^1E_1 states computed at 2.31 and 2.83 eV, respectively. In the solution spectra of $Zr(OEP)_2$ and $Ce(OEP)_2$ the features underlying the Q″ band are not clearly distinguishable. However, by analogy with $Th(OEP)_2$, it seems reasonable to associate the lower of the two ligand-centered states computed in the Q″ region to the lower energy side of the Q″ band, the higher to the higher energy side of this band.

The additional RMCT states predicted, both at BP and SAOP levels, in the Q″ band region of $Ce(P)_2$, some of which with appreciable intensity, should also contribute to the high-energy side of the Q″ band which in $Ce(OEP)_2$ extends to the red tail of the B band.

It is worth noting that in all three investigated $M(P)_2$ sandwiches the lower Q″ state is a nearly 50−50 mixture of the $11a_1 \rightarrow 16(17)e_1$ and $5b_1 \rightarrow 15(16)e_3$ transitions, with a minor contribution of the $11b_2 \rightarrow 15(16)e_3$, whereas the higher Q″ state is almost entirely described by the $14e_2 \rightarrow 15(16)e_3$ transition. The latter does not belong to the Gouterman a_{1u}, $a_{2u} \rightarrow e_g$* excitations, but has totally different character (excitation out of an "e_x" orbital). The character of these Q″ states is the same in the case of octaethyl substitution, i.e., for $Zr(OEP)_2$.

The very low oscillator strength computed for the lower Q″ state in all members of the series is due to opposite directions of the two large transition dipoles of the $5b_1 \rightarrow 15(16)e_3$ and $11a_1 \rightarrow 16(17)e_1$ transitions. Although the Q″ band is in the $M(OEP)_2$ sandwiches much weaker than the Q(0,0) band, the oscillator strengths calculated for the lower Q″ state in the model $M(P)_2$ systems seem to be somewhat underestimated. The experimental relative intensities of the Q and Q″ bands are however better reproduced when we take into account the alkyl substituents. Calculations on $Zr(OEP)_2$ show indeed that the β-ethyls induce an increase of the oscillator strength of the 3^1E_1, Q″ state, which is predicted in $Zr(OEP)_2$ about 30 times larger than in $Zr(P)_2$ (0.0029 vs 0.0001). The ethyl groups introduce very minor changes in the relative energies of the eight frontier orbitals; nevertheless they are sufficient to cause a less complete mixing of the $11a_1 \rightarrow 16e_1$ and $5b_1 \rightarrow 15e_3$ transitions and hence a less complete cancellation of the associated transition dipole moments. The intensities are obviously very sensitive to subtle chemical modifications of the ring systems.

According to the model by Holten et al.[4] the Q″ band is accounted for by the two CR$^+$ states:

$$CR_1{}^+ = [(b_1e_3) - (a_2e_1)]/\sqrt{2}$$

$$CR_2{}^+ = [(b_1e_3) - (a_2e_1)]/\sqrt{2}$$

In the limit of the degeneracy of the a_{1u}- and a_{2u}-derived configurations these states are degenerate, but will split in energy if the degeneracy is lifted, as is believed to occur in the symmetric OEP-substituted complexes. The splitting of the two CR$^+$ states is in this model invoked to explain the splitting of the Q″ absorption observed in the low-temperature spectrum of $Th(OEP)_2$.

Our calculations show that the splitting of the Q″ absorption is not related to the lifting of degeneracy of the four E_1 configurations involving the eight frontier orbitals; rather it is due to the presence of two excited states in this region, the higher lying of which is dominated by a transition out of a lower lying orbital, $14e_2$, to the eg*-derived $15e_3$. The lower one contains basically only two of the four configurations, the $11a_1 \rightarrow 16e_1$ and $5b_1 \rightarrow 15e_3$, and, in disagreement with the model by Holten et al., has a mixed EX/CR character in all systems, with the EX/CR parentage varying from 50/50 in zirconium to 49/51 in cerium and 57/43 in thorium.

(4d) B Band Region. The most intense feature in the optical spectra of M^{IV} bis(porphyrin) sandwiches is the near-UV B band, or B(0,0) band, which is slightly blue shifted from the position in the corresponding mono(porphyrin) complexes of the same macrocycles.

According to the computed excitation energies and oscillator strengths, the B(0,0) band of $Zr(OEP)_2$ at 3.24 eV and of $Th(OEP)_2$ at 3.23−3.24 eV is assigned to the 7^1E_1 excited state computed for $Zr(P)_2$ at 3.39 eV with oscillator strength of 1.5338 and for $Th(P)_2$ at 3.52 eV with oscillator strength of 2.002 (see Tables 4 and 5, respectively). The B(0,0) band of $Ce(OEP)_2$ at 3.28 eV is well accounted for by the 26^1E_1 excited state computed for $Ce(P)_2$ at 3.50 eV with an oscillator strength of 0.5418 (see Table 7). Although the energy of the B band computed for the model $M(P)_2$ systems is in satisfactory agreement with the experimental band maxima measured for the $M(OEP)_2$ sandwiches, nevertheless our calculations on $Zr(OEP)_2$ show that the agreement with the experiment sensibly improves when the β-ethyl substituents are included in the calculations (cf. Table 4).

The B state has a pronounced multitransition character. The four transitions involving the eight frontier orbitals all enter, although with different weights, in the composition of this state. They strongly mix however with other transitions, i.e., the $\pi \rightarrow \pi^*$ $10b_2 \rightarrow 15(16)e_3$ (in all $M(P)_2$ systems), the $\pi(e_x) \rightarrow d_\sigma$ $15e_1 \rightarrow 12a_1$ and also the $\pi(e_x) \rightarrow \pi^*$ $15e_1 \rightarrow 15e_3$ (in $Zr(P)_2$), and the $\pi \rightarrow f_\delta$ $12e_3 \rightarrow 15e_2$ (in $Ce(P)_2$). Actually the $\pi \rightarrow f_\delta$ $12e_3 \rightarrow 15e_2$ has the largest weight in the B state of $Ce(P)_2$. It is worth mentioning that also at SAOP level a RMCT $\pi \rightarrow f_\delta$ transition is found to dominate (56%) the B state of $Ce(P)_2$, although, due to the upshift of the f orbitals, this transition is out of a higher lying π orbital, $15e_1$.

Analysis of the (approximate) wave function of the B state of $Zr(P)_2$ and $Th(P)_2$ in terms of excitonic, charge resonance, and RMCT contributions reveals that this state has a mixed EX/CR/RMCT character (66/15/19 in zirconium, 68/17/14 in thorium), although the excitonic parentage is by far the largest. Not so is in $Ce(P)_2$ where the RMCT character is about 50%.

In $Zr(P)_2$ and $Th(P)_2$ the oscillator strength of the B state is very large. The reason is that the transition dipole moments of the four configurations with large dipole matrix elements, $(5a_116e_1)$, $(11a_116e_1)$, $(5b_115e_3)$, and $(11b_215e_3)$, and the transition dipole moment of the configuration $(10b_215e_3)$ with smaller but not negligible dipole matrix element (~ 1.61 au) all have parallel directions. In $Zr(P)_2$ the transition dipole moment of the $15e_1 \rightarrow 12a_1$ RMCT transition, which also enters to some extent (11%) in the composition of the B state, subtracts, resulting in the oscillator strength of the B state being in $Zr(P)_2$ somewhat smaller than in $Th(P)_2$.

In $Ce(P)_2$ the configurations with large dipole matrix elements, $(5a_217e_1)$, $(11a_117e_1)$, $(5b_116e_3)$, $(11b_216e_3)$, and $(10b_216e_3)$, account only for 31% for the composition of this state. Their transition dipole moments, although they interfere constructively, as in the case of $Zr(P)_2$ and $Th(P)_2$, are therefore relatively small, to the effect that the oscillator strength of the B state is in $Ce(P)_2$ significantly smaller than in the other members of the series.

In the red tail of the B band we compute several allowed excited states which have low oscillator strength but one, 5^1E_1 in $Zr(P)_2$ and $Th(P)_2$ and 22^1E_1 in $Ce(P)_2$. This relatively intense $^1E_1$ state is a ligand centered state in zirconium and thorium complexes, but is in $Ce(P)_2$, just as most of the $^1E_1$ states lying in the red tail of the Soret band, a purely RMCT state, being a nearly 50–50 mixture of the $11a_1 \rightarrow 16e_1$ and $5b_1 \rightarrow 15e_3$ transitions.

It is worth mentioning that also in $Zr(P)_2$ RMCT states come into play into the red tail of the B band. As a matter of fact, due to the presence of the low-lying $4d_\sigma$ $12a_1$ orbital in the virtual spectrum, the $11b_2 \rightarrow 12a_1$ ($\pi \rightarrow d_\sigma$) RMCT transition mixes with the $15e_1 \rightarrow 15e_3$ ($\pi \rightarrow \pi^*$) transition in the 1^1B_2 and 2^1B_2 excited states calculated in the red tail of the B band.

(4e) Triplet Excited States. In view of the relevance of triplet excited states for the photophysical properties of bis(porphyrin) sandwiches, the lowest dipole allowed triplet states have also been studied for all members of the series. The results for $Zr(P)_2$ and $Th(P)_2$ are collected in Table 8. Cerium(IV) bisporphyrins are nonluminescent,[2,17] and hence there is no experimental information on the triplet excited states. Nevertheless the lowest triplet excited states of cerium bis(porphyrin) sandwiches, a plethora of which of RMCT character are calculated in the 700–

Table 8. Calculated Excitation Energies (eV) for the Lowest Triplet Excited States of $Zr(P)_2$ and $Th(P)_2$[a]

	$Zr(P)_2$			$Th(P)_2$	
state	composition (%)	excitation energy	state	composition (%)	excitation energy
1^3E_3	100 ($5a_2 \rightarrow 15e_3$)	1.42	1^3E_3	99 ($5a_2 \rightarrow 15e_3$)	1.60
2^3E_3	98 ($11a_1 \rightarrow 15e_3$)	1.73	2^3E_3	97 ($11a_1 \rightarrow 15e_3$)	1.69
1^3E_1	95 ($11b_2 \rightarrow 15e_3$)	1.81	1^3E_1	90 ($11b_2 \rightarrow 15e_3$)	1.82
2^3E_1	98 ($5a_2 \rightarrow 16e_1$)	1.87	2^3E_1	95 ($5a_2 \rightarrow 16e_1$)	1.95
3^3E_1	96 ($11a_1 \rightarrow 16e_1$)	2.21	3^3E_1	90 ($11a_1 \rightarrow 16e_1$)	2.08
4^3E_1	98 ($5b_1 \rightarrow 15e_3$)	2.29		9 ($11b_2 \rightarrow 15e_3$)	
3^3E_3	98 ($11b_2 \rightarrow 16e_1$)	2.30	3^3E_3	98 ($11b_2 \rightarrow 16e_1$)	2.21
4^3E_3	64 ($14e_2 \rightarrow 15e_3$)	2.73	4^3E_1	96 ($5b_1 \rightarrow 15e_3$)	2.23
	35 ($5b_1 \rightarrow 16e_1$)		4^3E_3	98 ($5b_1 \rightarrow 16e_1$)	2.57
5^3E_1	98 ($14e_2 \rightarrow 15e_3$)	2.74	5^3E_1	98 ($14e_2 \rightarrow 15e_3$)	2.73
5^3E_3	65 ($5b_1 \rightarrow 16e_1$)	2.76	5^3E_3	97 ($14e_2 \rightarrow 15e_3$)	2.73
	35 ($14e_2 \rightarrow 15e_3$)		6^3E_1	91 ($10b_2 \rightarrow 15e_3$)	3.04
6^3E_1	98 ($10b_2 \rightarrow 15e_3$)	2.97		7 ($14e_2 \rightarrow 16e_1$)	
6^3E_3	97 ($14e_2 \rightarrow 16e_1$)	3.20	6^3E_3	97 ($14e_2 \rightarrow 16e_1$)	3.09
7^3E_1	98 ($14e_2 \rightarrow 16e_1$)	3.21	7^3E_1	91 ($14e^2 \rightarrow 16e_1$)	3.09
				8 ($10b_2 \rightarrow 15e_3$)	
			7^3E_3	65 ($10b_2 \rightarrow 16e_1$)	3.36
				33 ($10a_1 \rightarrow 15e_3$)	

[a] The major one-electron transitions contributing to the BP/ALDA solution vectors are also given; Gouterman orbitals are printed in italics.

2000 nm (1.8–0.7 eV) region for $Ce(P)_2$ (not reported in Table 8) may still play a role in the rapid radiationless decay observed upon excitation in the Q band.

The lowest triplet state of $Zr(P)_2$ and $Th(P)_2$ is found to be the 1^3E_3 state for which we compute a vertical excitation energy $(S_0 \rightarrow T_1)$ of 1.42 and 1.60 eV, respectively. The shift to the blue as the inter-ring separation increases parallels that predicted and observed for the corresponding 1^1E_3 Q′ state. Phosphorescence spectra of zirconium bis(porphyrin) sandwiches have not been published, to our knowledge, so there are no experimental data to which to compare the $S_0 \rightarrow T_1$ excitation energy we compute for $Zr(P)_2$.

As for thorium bis(porphyrin) sandwich complexes, they show phosphorescence between 900 and 1000 nm.[4] In the emission spectra the phosphorescence band is broad with a maximum at ~ 960 nm (~ 1.29 eV) in $Th(OEP)_2$ and at ~ 900 nm (~ 1.38 eV) in $Th(TPP)_2$.[4] Because the 1^3E_3 state in $Th(P)_2$ is, just like the corresponding 1^1E_3 (Q′) state, largely derived from the promotion of one electron from the antibonding $5a_2$ (HOMO) to the bonding $15e_3$ (LUMO), the potential energy curve of this state along the intermacrocycle distance coordinate should be displaced to shorter bond distance, relative to the ground state. Full optimization of $Th(P)_2$ in the 1^3E_3 state shows that this is actually the case (the $Th-N_{center}$ distance, i.e., the distance from the metal to the center-of-gravity for the eight coordinated pyrrolic nitrogens shortens by 0.016 Å). This implies that the most probable Franck–Condon transition, which corresponds to the phosphorescence peak in the emission spectrum, is shifted from the 0–0 origin to lower frequencies, and therefore it does not represent the origin of the 1^3E_3 state. Similar arguments led Holten et al.[4] to the same conclusions. These authors quote for $Th(OEP)_2$ the origin of the phosphorescent triplet state at about 810 nm (1.53 eV), a value which is very close to both the vertical (1.60 eV) and adiabatic (1.58 eV) $S_0 \rightarrow T_1$ excitation energies we compute for $Th(P)_2$.

The triplet–triplet absorption spectra of zirconium and thorium bis(porphyrin) sandwiches show a broad and intense induced T_1-T_n near-IR absorption.[4] Taking into account the

energy of the T_1 (1^3E_3) state, the broad near-IR absorption is well accounted for by transitions from the phosphorescent state to the higher triplet states of E_1 and E_3 symmetry located in the range of 2.3−2.8 eV. Thus, for example, the $1^3E_3{\rightarrow}5^3E_1$, 5^3E_3 transitions are predicted to occur in Zr(P)$_2$ at ∼930 nm and in Th(P)$_2$ at ∼1100 nm, in very nice agreement with the intense absorption observed near 930 nm and to the red of ∼1000 nm in the triplet−triplet absorption spectra of Zr(TPP)$_2$ [3] and Th(OEP)$_2$,[4] respectively.

The dipole allowed $1^3E_3{\rightarrow}7^3E_1$ and the dipole forbidden $1^3E_3{\rightarrow}7^3E_3$ transitions predicted to occur in Th(P)$_2$ at 832 nm (1.49 eV) and 704 nm (1.76 eV), respectively, nicely account for the two monoporphyrin-like features, the prominent absorption near 775 nm and the smaller absorption ∼1500 cm^{-1} to the blue, observed in the triplet−triplet absorption spectrum of Th(OEP)$_2$.[4]

5. Conclusions

We conclude that the time-dependent DFT calculations achieve a very gratifying agreement with the experimental excitation energies, and a reasonable qualitative picture of the associated intensities. The orbital splitting, due to ring−ring interactions, of the Gouterman a_{1u} and a_{2u} orbitals is different from what has been assumed before, but also the splitting which we calculate is basically simple: the a_{1u} orbitals on the two rings strongly overlap at the staggering angle of 45° and exhibit considerable splitting, the a_{2u} orbitals overlap little and split little. Apparently, this orbital level spectrum leads to excitation energies that can explain the experimental spectrum very well. However, it does not lead to a classification of the excited states, and hence of the bands in the spectrum, as purely excitonic excitations (intra-ring excitations that combine weakly with the equivalent one on the other ring) or purely charge-resonance excitations (ring-to-ring). Although the Q and B bands in the spectrum look similar to the ones known for the monomer porphyrin rings, we do not find the underlying excited states to conform to the expectation of being basically monomer excitations.

JA020554X